NOVA SCHOOL OF SCIENCE & TECHNOLOGY

DEPARTMENT OF LIFE SCIENCES

BEATRIZ DA CONCEIÇÃO ARAÚJO

BSc in Biochemistry

GENERATION OF AN HFpEF *IN VITRO* MODEL USING hiPSC-DERIVED CARDIAC ORGANOIDS

MASTER IN MOLECULAR GENETICS AND BIOMEDICINE

NOVA University Lisbon

September, 2025

NOVA SCHOOL OF SCIENCE & TECHNOLOGY

DEPARTAMENT OF LIFE SCIENCES

GENERATION OF AN HFpEF *IN VITRO* MODEL USING hiPSC-DERIVED CARDIAC ORGANOIDS

BEATRIZ DA CONCEIÇÃO ARAÚJO

BSc in Biochemistry

Adviser: José António Henriques de Conde Belo
Full Professor, NOVA Medical School, NOVA University Lisbon

Co-adviser: Paula Alexandra Quintela Videira
Associate Professor, NOVA School of Science and Technology (FCT-NOVA), NOVA University Lisbon

Examination Committee:

Chair: Maria Alexandra Núncio de Carvalho Ramos Fernandes,
Full Professor, FCT-NOVA, NOVA University Lisbon

Rapporteur: Henrique Vazão de Almeida,
Assistant Researcher, FCT-NOVA, NOVA University Lisbon

Adviser: José António Henriques de Conde Belo,
Full Professor, NOVA Medical School, NOVA University Lisbon

Members: José António Henriques de Conde Belo,
Full Professor, NOVA Medical School, NOVA University Lisbon
Henrique Vazão de Almeida,
Assistant Researcher, FCT-NOVA, NOVA University Lisbon

MASTER IN MOLECULAR GENETICS AND BIOMEDICINE

NOVA University Lisbon
September, 2025

Generation of an HFpEF *in vitro* model using hiPSC-derived cardiac organoids

A todos os que me apoiaram ao longo deste percurso.

The work developed during this Master's Thesis originated:

- José Manuel Inácio, Micael Almeida, Carlos Vital, Beatriz Araújo, and José António Belo. Modeling Cardiac Disease Using Patient-Derived and Gene-Edited iPSCs Technologies. CorEuStem 2025, May 29-30, 2025, Milan, Italy. [Poster and Oral Presentation by José Manuel Inácio]
- José Manuel Inácio, Micael Almeida, Carlos Vital, Beatriz Araújo and José António Belo. Using *in vivo* and cellular models for the study of human cardiac disease. LS4FUTURE 2nd General Meeting, July 1, Oeiras, Portugal. [Poster Presentation]

ACKNOWLEDGMENTS

Gostaria de começar por agradecer ao Professor José Belo por me ter recebido no Laboratório de Células Estaminais e Desenvolvimento e me ter proporcionado a oportunidade de realizar a minha tese de mestrado, que me permitiu aprender tanto.

À Professora Paula Videira, um grande agradecimento por ter aceite ser minha co-orientadora neste projeto e pela ajuda prestada.

Ao Zé, gostava de deixar um especial agradecimento por todo o apoio que me deu ao longo deste ano e por me ter feito olhar para a ciência de outra forma. A tua calma, resiliência e boa energia fizeram com que esta experiência fosse muito enriquecedora. O que aprendi contigo, vou levar para a vida. Palavras não chegam para te agradecer por tudo.

Aos meus colegas de laboratório, agradeço por terem contribuído para um ambiente leve e de entreajuda. A vossa companhia, positividade e boa disposição tornaram cada dia mais fácil. Em especial, um enorme obrigada ao Carlos, pela sua paciência, disponibilidade e incansável apoio desde o primeiro dia. Foste uma peça fundamental nesta experiência.

Um agradecimento à NOVA School of Science and Technology, onde adquiri a base teórica e me apaixonei pela ciência, e à NOVA Medical School Research onde o trabalho experimental de tese decorreu. Gostaria ainda de agradecer às Infraestruturas de Cultura Celular, Microscopia e Histologia da NOVA Medical School Research, sem as quais não teria sido possível realizar este trabalho.

À minha família, especialmente aos meus pais, irmã e namorado, agradeço por terem estado sempre ao meu lado e terem sempre acreditado em mim. Este trabalho também vos pertence. Aos meus amigos, especialmente à Cate, Clara, Luísa, Mariana e Rafaela deixo também um agradecimento por terem sempre estado aqui para mim.

This work was funded by MPS_NOVA (Microphysiological Systems) and iNOVA4Health under the projects HORIZON-WIDERA-2023-ACCESS Nº 101159729 and iNOVA4Health-UID/Multi/04462/2020, respectively.

ABSTRACT

Heart failure with preserved ejection fraction (HFpEF) affects over 32 million people worldwide, with fibrosis representing a key underlying mechanism. Effective therapies remain lacking due to the challenge of establishing HFpEF models. A recent study from our laboratory identified miRNA-mRNA interactions potentially relevant to HFpEF and validated them in 2D cardiomyocyte cultures: *Hyaluronan and Proteoglycan Link Protein 1* (*HAPLN1*) was downregulated by hsa-miR-25-3p and hsa-miR-26a-5p, while *Natriuretic Peptide B* (*NPPB*) was downregulated by hsa-miR-26a-5p. Although human induced pluripotent stem cell (hiPSC)-based cardiac models are useful tools for studying cardiac disease, 2D systems do not replicate the complexity of *in vivo* (patho)physiology. To overcome this, hiPSC-derived cardiac organoids have emerged as a promising alternative.

hiPSC-derived human cardioids that recapitulate essential structural and functional features of the native heart were generated in the frame of this work. Here, I aimed to advance the establishment of a reliable HFpEF *in vitro* model by addressing the potential role of hsa-miR-25-3p and hsa-miR-26a-5p in myocardial stiffness, using hiPSC-derived cardioids. The suitability of cardioids for studying fibrosis-related mechanisms was demonstrated by cardiac fibroblast (CF) activation, evidenced by increased α-smooth muscle actin (α-SMA) expression, as well as by extracellular matrix (ECM) accumulation, evidenced by a statistically significant increase in collagen deposits following Transforming Growth Factor β (TGF-β) treatment. miRNA delivery into cardioids was optimized, with a liposomal-based approach using 1 μM miRNA and serum supplementation after complex formation as the most effective condition, ensuring distribution throughout the inner regions of the cardioid for six days. Repeated delivery of hsa-miR-25-3p and hsa-miR-26a-5p reduced *HAPLN1* expression in one cardioid batch, although no significant overall reduction was observed for either *HAPLN1* or *NPPB*. Under the same conditions, CF activation was promoted, although not significantly. ECM deposition did not increase significantly following the delivery of the miRNAs.

Altogether, this work demonstrates that our cardioid model effectively recapitulates features of the human heart and is a suitable platform to investigate fibrosis-associated mechanisms, supporting its potential as an HFpEF model. Moreover, we established a protocol for miRNA delivery into 3D cardiac systems. Further studies are required to confirm the downregulation of *HAPLN1* and *NPPB* by hsa-miR-25-3p and hsa-miR-26a-5p in cardioids, as well as to clarify their role in modulating CF activation and ECM deposition, processes that contribute to myocardial stiffness in HFpEF.

Keywords: HFpEF, human cardioids, miRNAs, fibrosis

RESUMO

A insuficiência cardíaca com fração de ejeção preservada (ICFEP) afeta mais de 32 milhões de pessoas em todo o mundo, sendo a fibrose um dos principais mecanismos subjacentes. Continuam a faltar terapias eficazes devido à dificuldade em estabelecer modelos de ICFEP. Um estudo recente do nosso laboratório identificou interações miRNA-mRNA potencialmente relevantes para ICFEP e validou-as em culturas 2D de cardiomiócitos: *Hyaluronan and Proteoglycan Link Protein 1* (*HAPLN1*) foi regulado negativamente por hsa-miR-25-3p e hsa-miR-26a-5p, enquanto *Natriuretic Peptide B* (*NPPB*) foi regulado negativamente por hsa-miR-26a-5p. Embora os modelos cardíacos baseados em células estaminais pluripotentes induzidas humanas (hiPSCs) sejam úteis para o estudo de doenças cardíacas, os sistemas 2D não reproduzem a complexidade das condições (pato)fisiológicas *in vivo*. Para ultrapassar esta limitação, organoides cardíacos derivados de hiPSCs surgiram como uma alternativa promissora.

Cardioides humanos derivados de hiPSCs que recapitulam características estruturais e funcionais essenciais do coração nativo foram gerados neste trabalho. Procurei contribuir para o estabelecimento de um modelo *in vitro* fiável de ICFEP, explorando o potencial papel de hsa-miR-25-3p e hsa-miR-26a-5p na rigidez miocárdica, utilizando cardioides derivados de hiPSCs. A adequação dos cardioides para o estudo de mecanismos relacionados com a fibrose foi demonstrada pela ativação de fibroblastos cardíacos (FCs), comprovada pelo aumento da expressão de α-smooth muscle actin (α-SMA), assim como pela acumulação de matriz extracelular (MEC), comprovada por um aumento estatisticamente significativo de depósitos de colagénio após tratamento com Transforming Growth Factor β (TGF-β). A entrega de miRNA aos cardioides foi otimizada, sendo a abordagem baseada em lipossomas utilizando 1 μM de miRNA e suplementação com soro após a formação do complexo a mais eficaz, assegurando a distribuição para as regiões internas do cardioide durante seis dias. A entrega repetida de hsa-miR-25-3p e hsa-miR-26a-5p reduziu a expressão de *HAPLN1* num dos lotes de cardioides, embora, no geral, não tenham sido observadas reduções significativas na expressão de *HAPLN1* nem de *NPPB*. Nas mesmas condições, ativação de FCs foi promovida, embora sem significância estatística. A deposição de MEC também não aumentou de forma significativa após a entrega dos miRNAs.

Em conjunto, este trabalho demonstra que o nosso modelo de cardioide recapitulou de forma eficaz características do coração humano e que constitui uma plataforma adequada para o estudo de mecanismos associados à fibrose, reforçando o seu potencial como modelo de ICFEP. Além disso, foi estabelecido um protocolo de entrega de miRNA em sistemas cardíacos 3D. Estudos futuros são necessários para confirmar a regulação negativa de *HAPLN1* e *NPPB* por hsa-miR-25-3p e hsa-miR-26a-5p em cardioides e clarificar o seu papel na ativação de FCs e deposição de MEC, processos que contribuem para a rigidez miocárdica na ICFEP.

Palavras-chave: ICFEP, cardioides humanos, miRNAs, fibrose

TABLE OF CONTENTS

LIST OF FIGURES

LIST OF TABLES

LIST OF ABBREVIATIONS

2D - Two-dimensional
3′ UTR - 3′ untranslated region
3D - Three-dimensional
BMP4- Bone morphogenic protein 4
BNP - B-type natriuretic peptide
BS - Blocking solution
BSA - Bovine serum albumin
cDNA - Complementary deoxyribonucleic acid
CFs - Cardiac fibroblasts
CMECs - Coronary microvascular endothelial cells
CMFs - Cardiac myofibroblasts
CMs - Cardiomyocytes
COL1A1 - α1 chain of type I collagen
DAPI - 4′,6-diamidino-2-phenylindole
DMEM/F12 - Dulbecco's Modified Eagle's Medium/Nutrient Mixture F-12
DPBS - Dulbecco's Phosphate Buffered Saline
DS - Donkey serum
E8 - Essential 8 Flex medium
ECM - Extracellular matrix
ECs - Endothelial cells
ERK/MAPK - Extracellular signal-regulated kinase/Mitogen-activated protein kinase
ESCs - Embryonic stem cells
FBS - Fetal bovine serum
FGF - Fibroblast growth factor
FMT - Fibroblast-to-myofibroblast transition
HA - Hyaluronic acid
HAPLN1 - Hyaluronan and Proteoglycan Link Protein 1

hESC - Human embryonic stem cell
HF - Heart failure
HFmrEF - Heart failure with mildly reduced ejection fraction
HFpEF - Heart failure with preserved ejection fraction
HFrEF - Heart failure with reduced ejection fraction
hiPSC - Human induced pluripotent stem cell
hPSCs - Human pluripotent stem cells
iPSCs - Induced pluripotent stem cells
LV - Left ventricle
LVEF - Left ventricular ejection fraction
LVFPs - Left ventricular filling pressures
mESCs - Mouse embryonic stem cells
miRISC - MicroRNA-induced silencing complex
miRNA - micro ribonucleic acid
MMPs - Matrix metalloproteases
MREs - miRNA response elements
mRNA - Messenger ribonucleic acid
MT - Masson's Trichrome
NaN_3 - Sodium azide
NPPB - B-type natriuretic peptide gene
PAI-1 - Plasminogen-activator inhibitor-1
PBS - Phosphate-buffered saline
PBS-Triton – Phosphate-buffered saline with Triton X-100
PFA - Paraformaldehyde
PI3K/AKT - Phosphatidylinositol-3-kinase/V-akt murine thymoma viral oncogene homolog
Pre-miRNAs - Precursor miRNAs
Pri-miRNAs - Primary miRNAs
PSCs - Pluripotent stem cells
PTEN - Tumor suppressor phosphatase and tensin homolog
RB without vitamin A - RPMI Medium 1640 supplemented with B27 without vitamin A
RB- - RPMI Medium 1640 supplemented with B27 without insulin
RhoA/ROCK - Ras homolog gene family member A/Rho-associated coiled-coil containing protein kinase
RNA - Ribonucleic acid
RT - Room temperature
RT-qPCR - Real-time quantitative polymerase chain reaction
SMAD - Small Mothers Against Decapentaplegic

SMAD7 - Small Mothers Against Decapentaplegic 7
SPRY1 - Sprouty homolog 1
TGF-β - Transforming Growth Factor β
TIMPs - Tissue inhibitors of metalloproteases
VCAM-1 - Vascular cell adhesion molecule-1
VE-Cadherin - Vascular endothelial cadherin
VEGF - Vascular endothelial growth factor
***α*-SMA** - α-smooth muscle actin

1

INTRODUCTION

1.1 Heart failure with preserved ejection fraction

The heart is responsible for supplying oxygen and nutrients to the peripheral tissues through the blood. When this organ is unable to pump blood at an adequate rate or can do so only at the expense of elevated left ventricular filling pressures (LVFPs), it enters a pathological state clinically defined as heart failure (HF) [1]. HF represents a leading cause of mortality and disability, affecting over 64 million people worldwide, corresponding to approximately 1% to 2% of the global population [2], [3]. This complex clinical syndrome is characterized by typical symptoms and signs resulting from structural and functional cardiac abnormalities, most commonly involving the left ventricle (LV), a heart chamber that relaxes during diastole to permit filling and contracts during systole to eject blood into systemic circulation [1], [4]. The European Society of Cardiology classifies HF into distinct types based on the left ventricular ejection fraction (LVEF), the fraction of blood volume ejected from the LV into systemic circulation per beat. These categories include heart failure with reduced ejection fraction (HFrEF), mildly reduced ejection fraction (HFmrEF), and preserved ejection fraction (HFpEF), corresponding to LVEF values of ≤40%, 41–49%, and ≥50%, respectively [2], [5].

Approximately 50% of all HF cases are classified as HFpEF, affecting around 32 million people worldwide [6]. This complex syndrome primarily affects the elderly, with a higher prevalence among women, and is commonly associated with multiple cardiac and non-cardiac co-morbidities, including obesity, hypertension, diabetes, chronic kidney disease, and chronic obstructive pulmonary disease, among others [6]. Within the affected population, different phenotypes with overlapping characteristics are observed, reflecting the heterogeneity of HFpEF [7]. To establish a definition, the European Society of Cardiology recently characterized this syndrome by a preserved LVEF (≥ 50%), together with typical signs and symptoms of HF,

such as elevated jugular venous pressure, pulmonary crackles, peripheral edema, breathlessness, exercise intolerance, and extreme fatigue. In addition, objective evidence of cardiac structural and/or functional abnormalities consistent with diastolic dysfunction/elevated LVFPs is required, such as elevated natriuretic peptide levels [4], [8].

Research suggests that HFpEF results from cardiac remodeling mechanisms involving alterations in cardiomyocytes (CMs) and the extracellular matrix (ECM) of the adult heart, with the LV being particularly affected – **Figure 1** [9]. These remodeling processes promote increased LV wall thickness and stiffness, reducing LV compliance and causing difficulty in the filling of this heart chamber during diastole - a condition referred to as diastolic dysfunction, a hallmark of HFpEF [7], [9]. In the early stages of HFpEF, diastolic dysfunction is evident only during exercise, when the LV requires higher filling pressures to maintain adequate blood volume. However, as the syndrome progresses, these elevated filling pressures persist even at rest, representing a key factor driving the symptoms of HFpEF [5], [10].

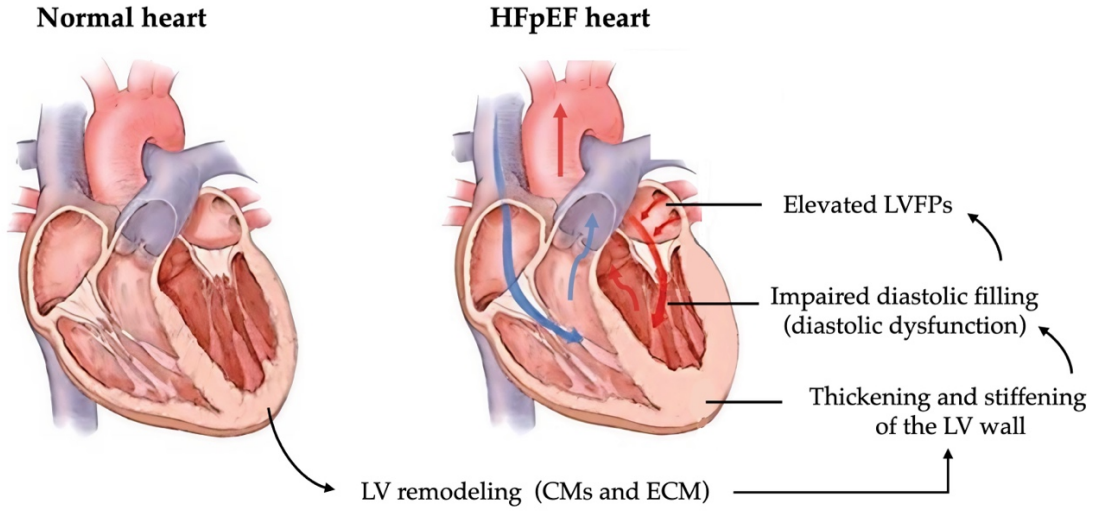

Figure 1: Structural and functional changes associated with HFpEF. Cardiac remodeling in heart failure with preserved ejection fraction (HFpEF) is driven by alterations in cardiomyocytes (CMs) and the extracellular matrix (ECM). These remodeling processes result in thickened and stiffer left ventricular (LV) walls, limiting LV relaxation during diastole. Consequently, the filling of this chamber is more difficult during diastole (diastolic dysfunction), as it is only possible at the cost of increased left ventricular filling pressures (LVFPs). Adapted from [11].

HFpEF is associated with elevated rates of hospitalization and mortality. Its prevalence is rising and is expected to keep increasing, largely due to the growing incidence of risk factors such as obesity and diabetes, as well as the aging of the global population [7], [12]. Despite the increasing burden of HFpEF, progress in the development of effective therapies remains limited, representing one of the most significant challenges in cardiology [7], [13]. A major obstacle contributing to this challenge is the heterogeneity of the syndrome, which makes it difficult to develop a reliable model for the identification of potential therapeutic targets [13], [14].

Given these limitations, the current therapeutic strategy focuses primarily on the rigorous control of underlying risk factors and the use of sodium-glucose cotransporter-2 inhibitors, which exert cardioprotective effects [15], [16].

1.1.1 Myocardial fibrosis as a pathological process in HFpEF

Myocardial fibrosis occurs in response to cardiac stress [17]. This process is characterized by the activation of cardiac fibroblasts (CFs) into cardiac myofibroblasts (CMFs) – cells with a remarkable capacity to synthesize and secrete large amounts of ECM proteins – as well as by the aberrant accumulation of these proteins within the tissue [17], [18], [19]. Fibrosis can be classified as either reactive or replacement – **Figure 2** [17].

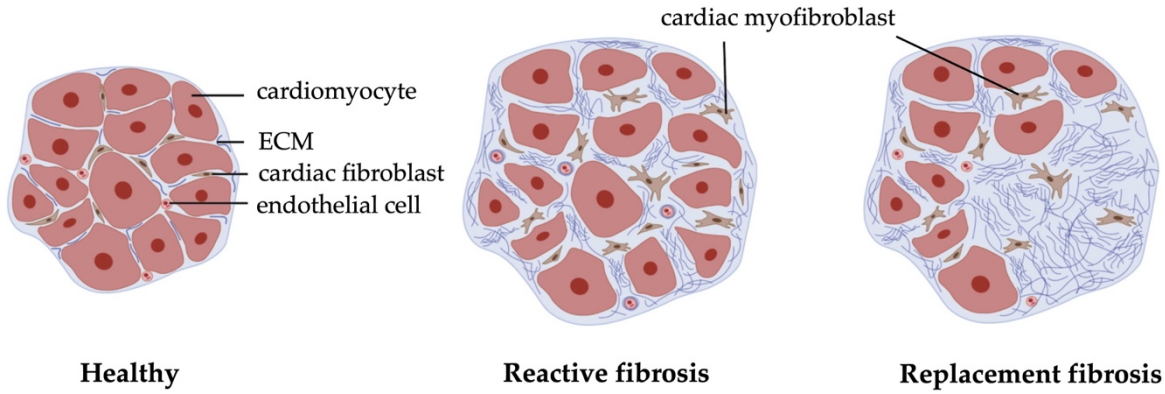

Figure 2: Types of fibrosis and their impact on myocardial architecture. In response to cardiac stress, cardiac fibroblasts (brown, elongated shape) are activated into cardiac myofibroblasts (brown, web-like shape). These cells synthesize and secrete large amounts of extracellular matrix (ECM) proteins (dark blue). In reactive fibrosis, this fibroblast activation and ECM deposition occur in response to chronic injury. In contrast, in replacement fibrosis, these processes follow acute injury, such as myocardial infarction, where the fibrotic scar replaces lost cardiomyocytes (red), preventing cardiac rupture. The excessive accumulation of ECM proteins alters normal tissue architecture in both types of fibrosis, compromising cardiac function. Adapted from [20].

Reactive fibrosis is typically associated with chronic cardiac conditions, such as HFpEF, and is characterized by the diffuse deposition of ECM proteins in the cardiac interstitium, in the absence of CM loss [17], [21]. In contrast, replacement fibrosis is part of the reparative response to CM loss, as occurs in myocardial infarction. In this case, a fibrotic scar forms to prevent cardiac rupture, since the heart's limited regenerative capacity does not allow adequate replacement of the damaged tissue with newly formed CMs [17], [22]. In both cases, the formation of fibrotic tissue alters normal tissue architecture, consequently impairing the heart's mechanical and electrical properties, nutrient diffusion, and cell-cell communication, impacting cardiac function [23], [24]. Although the mechanisms underlying HFpEF remain incompletely understood, research indicates that reactive myocardial fibrosis in this context is initiated by a systemic proinflammatory state driven by the comorbidities frequently

associated with the condition – **Figure 3**. It is suggested that prolonged exposure of coronary microvascular endothelial cells (CMECs) to inflammatory molecules leads to endothelial dysfunction, characterized by the generation of reactive oxygen species [9]. Furthermore, there is an upregulation of endothelial adhesion molecules, including E-selectin and vascular cell adhesion molecule-1 (VCAM-1), promoting the adhesion and transendothelial migration of immune cells, which, once in the myocardial tissue, release Transforming Growth Factor β (TGF-β) [9], [25], [26].

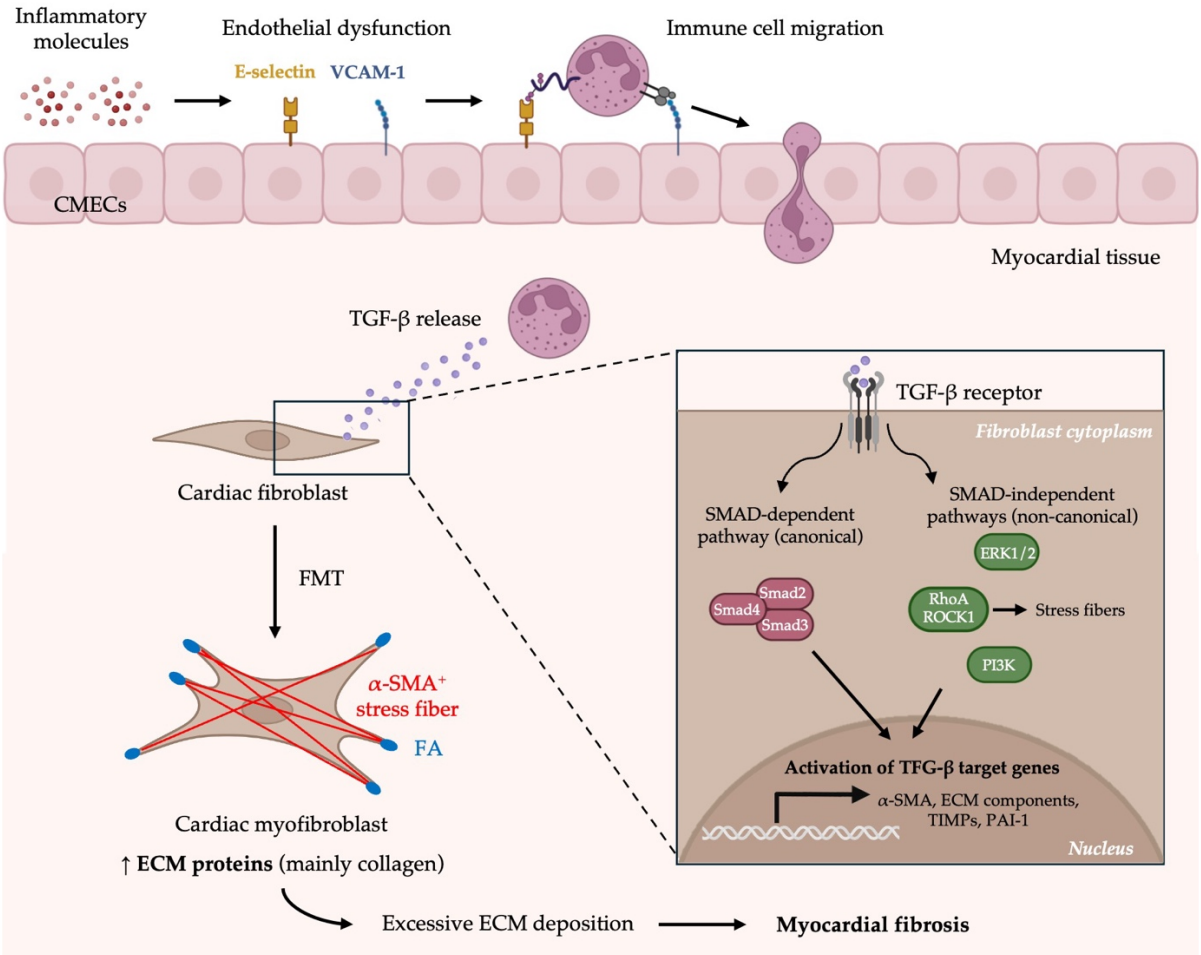

Figure 3: Molecular mechanisms underlying fibrosis in HFpEF. The prolonged exposure of coronary microvascular endothelial cells (CMECs) to inflammatory molecules (dark red) leads to endothelial dysfunction, characterized by the expression of adhesion molecules such as E-selectin (yellow) and vascular cell adhesion molecule-1 (VCAM -1; dark blue). Immune cells adhere to the endothelium and migrate through it, subsequently releasing Transforming Growth Factor β (TGF-β) molecules (purple), which bind to receptors (black and grey) on the surface of cardiac fibroblasts. Small Mothers Against Decapentaplegic (SMAD)-dependent (pink) and independent (green) pathways are activated, including the Extracellular signal-regulated kinase/Mitogen-activated protein kinase (ERK/MAPK) pathway, the Ras homolog gene family member A/Rho-associated coiled-coil containing protein kinase (RhoA/ROCK) pathway, and the phosphatidylinositol-3-kinase/V-akt murine thymoma viral oncogene homolog (PI3K/AKT) pathway, among others. The activation of these pathways leads to the expression of TGF-β target genes in the nucleus, including α-smooth muscle actin (α-SMA), extracellular matrix (ECM) components,

such as collagen, and ECM regulators, such as tissue inhibitors of metalloproteinases (TIMPs) and plasminogen activator inhibitor-1 (PAI-1). The cardiac myofibroblast resulting from fibroblast-to-myofibroblast (FMT) transition is characterized by α-SMA^{+} stress fibers (red), focal adhesions (light blue), and enhanced production, secretion, and stabilization of ECM proteins, whose excessive deposition leads to myocardial fibrosis. Adapted from [25], [27]. Created with Biorender.

This cytokine is a key regulator of the phenotypic transition of CFs into CMFs, a process termed fibroblast-to-myofibroblast transition (FMT) [19], [28]. TGF-β mediates this process through the activation of multiple molecular pathways, including Small Mothers Against Decapentaplegic (SMAD)-dependent and independent signaling cascades [19], [29]. These pathways promote the reorganization of the actin cytoskeleton into stress fibers and the up-regulation of α-smooth muscle actin (α-SMA), a contractile protein incorporated into the fibers along the FMT process [29], [30]. Moreover, these pathways promote the expression of structural ECM proteins, such as type 1 collagen, and favor matrix accumulation by limiting matrix metalloproteases (MMPs) activity and stimulating the production of protease inhibitors [19]. Additionally, TGF-β has been involved in the increase of collagen stability by promoting enhanced cross-linking [19]. As a result, fully activated CMFs exhibit prominent α-SMA-positive stress fibers, making α-SMA the most widely used marker of these cells, together with a heightened ability to produce, secrete, and stabilize ECM proteins, promoting their accumulation within the myocardial tissue [19], [23], [30]. In HFpEF patients, this activation process and excessive protein deposition occur particularly in the LV, driving pathological remodeling and playing a pivotal role in the pathogenesis of the syndrome [9], [19].

1.2 miRNAs

Micro ribonucleic acids (miRNAs) are an important class of endogenous, noncoding single-stranded ribonucleic acids (RNAs), typically averaging 22 nucleotides in length. First identified in *Caenorhabditis elegans* in 1993, these molecules are present in animals, plants, and some viruses [31], [32]. miRNAs act as powerful regulators of various cellular processes, including cell fate determination during development and control of the cell cycle [33].

In mammals, miRNAs are estimated to regulate approximately 30% of all protein-coding genes at the post-transcriptional level, by base pairing with target messenger ribonucleic acids (mRNAs), inhibiting their translation and promoting their degradation [34], [35]. The generation of mature miRNAs capable of such regulation begins in the nucleus, with the production of primary miRNAs (pri-miRNAs), which are long hairpin structures with imperfect base-pairing – **Figure 4** [34], [35]. These molecules are first processed by the enzyme Drosha into shorter precursor miRNAs (pre-miRNAs), which are then exported to the cytoplasm. There, they undergo further processing by the enzyme Dicer, resulting in a mature miRNA duplex

approximately 22 nucleotides in length. The miRNA duplex is loaded into the Argonaute protein, where the passenger strand is removed and the guide strand is retained, forming the core of the microRNA-induced silencing complex (miRISC) [35]. Through partial base pairing, primarily mediated by the 5′ seed region of the miRNA, the miRISC complex recognizes complementary sequences within the 3′ untranslated region (3′ UTR) of target mRNAs. This leads to the recruitment of silencing effectors that promote translational repression and mRNA degradation [32], [36].

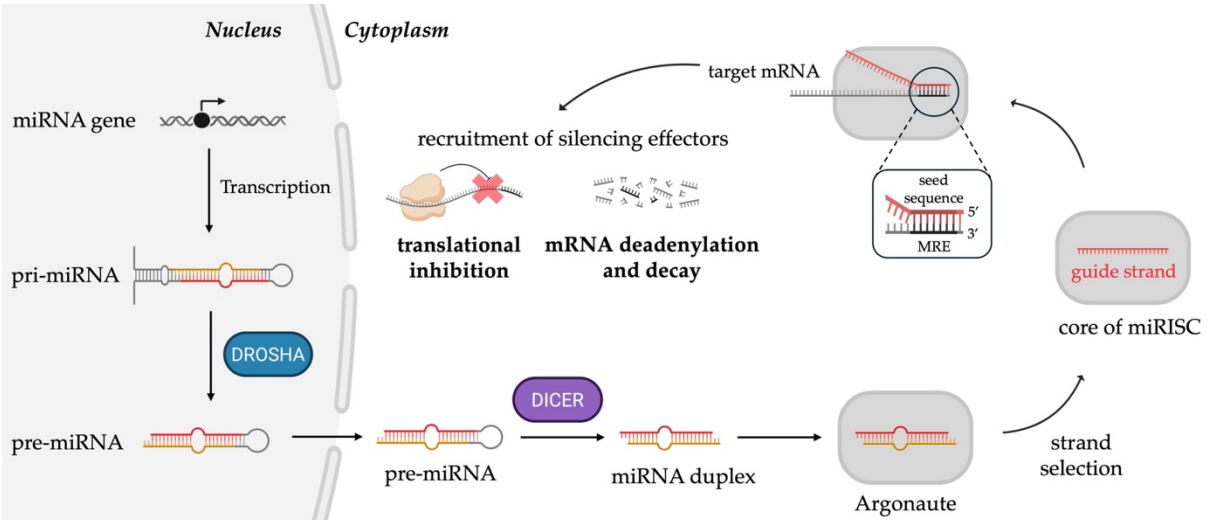

Figure 4: miRNA-mediated gene silencing. In the nucleus, miRNA genes are transcribed into primary microRNAs (pri-miRNAs), which are long hairpin structures with imperfect base pairing. These are processed by the RNase enzyme Drosha (blue), yielding ~70-nucleotide precursor microRNAs (pre-miRNAs). Pre-miRNAs are exported to the cytoplasm, where Dicer (purple), another RNase enzyme, cleaves them near the loop, producing a mature double-stranded miRNA duplex of ~22 nucleotides, consisting of a guide strand (red) and a passenger strand (yellow). The miRNA duplex is transferred to an Argonaute protein (light grey), where strand selection occurs: the guide strand is retained, while the passenger strand is degraded. Together, the guide strand and the Argonaute protein form the core of the microRNA-induced silencing complex (miRISC). The guide strand directs miRISC to its target mRNA (grey) by pairing its seed sequence (nucleotides 2-8 at the miRNA 5′ end; dark red) with complementary miRNA response elements (MREs) in the target mRNA's 3′ untranslated region (3′UTR; black). This base pairing leads to the recruitment of miRNA-mediated silencing effectors, which induce translational repression and promote mRNA deadenylation and decay. Adapted from [37]. Created with Biorender.

1.2.1 miRNAs in HFpEF

Distinct miRNA expression profiles have been associated with different HF subtypes, with circulating miRNAs emerging as promising biomarkers for their differentiation [38], [39]. However, the specific contributions of these miRNAs to the underlying pathophysiological processes are not yet fully clarified [39].

Nonetheless, miR-21 is one of the few extensively studied miRNAs in the context of HFpEF, where it is upregulated [39]. Accumulating evidence supports its involvement in the progression of the syndrome, particularly through its contribution to myocardial fibrosis [26], [39]. MiR-21 exerts its effects by downregulating multiple mRNA targets that act as key inhibitors of fibrosis-related signaling pathways [26], [40]. Examples include *Small Mothers Against Decapentaplegic 7* (*SMAD7), Sprouty homolog 1* (*SPRY1*), and *tumor suppressor phosphatase and tensin homolog* (*PTEN*) mRNA targets, which inhibit SMAD-dependent, ERK-MAPK, and PI3K/AKT cascades, respectively. By downregulating these inhibitors, miR-21 amplifies profibrotic signaling, thereby contributing to pathological cardiac remodeling [26], [40].

Recently, in our laboratory, novel miRNAs have been identified as potential contributors to the pathophysiology of HFpEF, as a result of their regulatory interactions with target mRNAs [15]. These include hsa-miR-25-3p, hsa-miR-26a-5p, and hsa-miR-4429, which were shown to downregulate *Hyaluronan and Proteoglycan Link Protein 1* (*HAPLN1*) mRNA, whereas hsa-miR-26a-5p and hsa-miR-140-3p were associated with the downregulation of *Natriuretic Peptide B* (*NPPB*) mRNA [15]. HAPLN1 plays an important role in assembling a hyaluronic acid (HA)-rich ECM by stabilizing the interaction between HA and proteoglycans. This ECM environment is crucial for proper heart development and post-injury tissue repair [15]. It has been shown that the depletion of $HAPLN1^{+}$ cells compromises CM and CF proliferation in zebrafish, thereby impairing heart regeneration following injury [15], [41]. *NPPB* mRNA encodes a precursor of B-type natriuretic peptide (BNP), a cardiac hormone secreted by the atrial and ventricular myocardium during heart development as well as by ventricular CMs in response to cardiac stress, as occurs in HF [42]. Under these conditions, BNP exerts a cardioprotective function by restoring blood volume and vascular tone to physiological levels [43]. Moreover, BNP has been demonstrated to exert antifibrotic effects in human CFs exposed to TGF-β [44].

1.3 Modeling cardiac development and disease

Much of our current understanding of human cardiac development and disease has been derived from studies using animal model organisms. These models have enabled the identification of key genetic regulators and signaling pathways involved in cardiogenesis, clarified the molecular mechanisms underlying cardiac pathologies, and contributed to the discovery of potential therapeutic targets, as reviewed in [45], [46].

The mouse, in particular, has become the most widely used animal model in developmental cardiology, owing to its genetic similarity to humans, comparable developmental processes, and ease of genetic manipulation [46], [47]. In contrast, disease modeling requires case-

specific selection of the animal model, as reviewed in [48]. In the context of HFpEF, several models have been developed by inducing one or more relevant comorbidities. Among these, the ZSF1 rat is widely used, as it reproduces HFpEF features, including endothelial dysfunction and diastolic dysfunction resulting from diabetes and hypertension [49], [50].

Despite the valuable insights gained from animal models, they present significant limitations, including ethical concerns and the challenge of extrapolating findings across species, which is evident, for example, in non-coding RNA (e.g., miRNAs) mechanisms, as these are often poorly conserved [15], [51], [52]. These constraints highlight the need for reliable, human cell-based models to study human cardiac development and disease. In this context, cardiac models derived from human pluripotent stem cells (hPSCs) have emerged as a promising alternative [52].

1.3.1 Human pluripotent stem cells

Pluripotent stem cells (PSCs) are defined by two fundamental properties: self-renewal, the capacity for unlimited proliferation while maintaining an undifferentiated state, and pluripotency, the ability to leave their undifferentiated state to become cells from all three germ layers of the developing embryo – ectoderm, mesoderm, and endoderm – thus enabling the generation of all cell types found in the adult organism. Examples of PSCs include embryonic stem cells (ESCs) and induced pluripotent stem cells (iPSCs) [53], [54] – **Figure 5.**

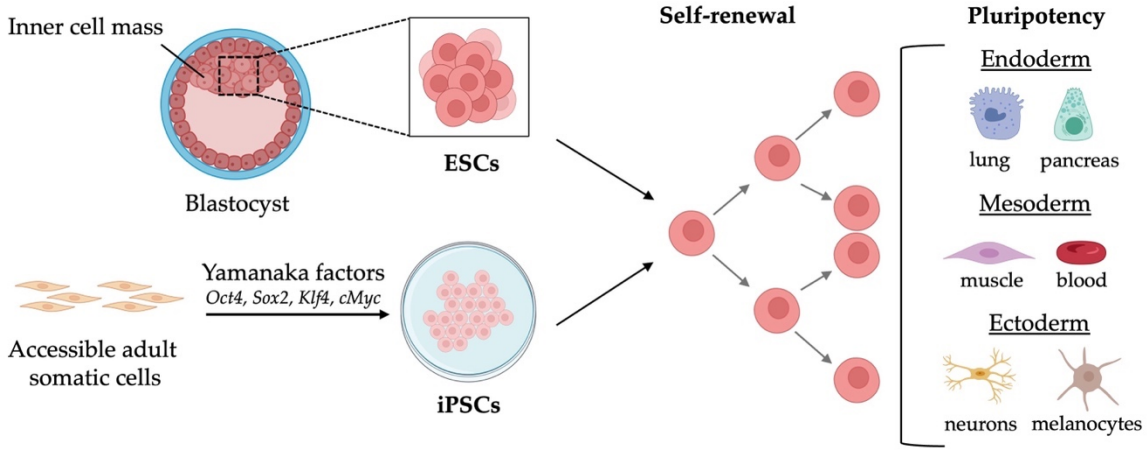

Figure 5: Origins and characteristics of pluripotent stem cells. Embryonic stem cells (ESCs) are derived from the inner cell mass of the blastocyst, while induced pluripotent stem cells (iPSCs) are generated by reprogramming accessible adult somatic cells, such as fibroblasts, through the introduction of the Yamanaka transcription factors (*Oct4*, *Sox2*, *Klf4*, and *cMyc*). Both ESCs and iPSCs are capable of self-renewal and pluripotency, allowing them to proliferate indefinitely while remaining undifferentiated and to differentiate into cells from all three germ layers: endoderm (e.g., lung epithelial cells, pancreatic cells), mesoderm (e.g., muscle cells such as cardiomyocytes, blood cells), and ectoderm (e.g., neurons, melanocytes). Created with Biorender.

ESCs are derived from the inner cell mass of the blastocyst during early mammalian development, the region that ultimately gives rise to the embryo. Cells from the inner cell mass can differentiate into all cell types of the adult organism, except those that form extra-embryonic tissues [53], [54]. The first ESCs to be isolated were mouse embryonic stem cells (mESCs) in 1981. In 1998, human ESCs were successfully derived from blastocysts generated through *in vitro* fertilization, marking the establishment of the first human embryonic stem cell (hESC) line [54], [55].

The development of iPSC technology has profoundly impacted *in vitro* research by providing cells with the dual advantages of self-renewal and pluripotency, enabling the generation of any cell type, while circumventing the ethical concerns associated with ESCs [55]. iPSCs are generated by reprogramming accessible adult somatic cells (e.g., fibroblasts or blood cells) into a pluripotent state through the introduction of four specific transcription factors: *Oct4*, *Sox2*, *Klf4*, and *cMyc*, collectively referred to as the Yamanaka factors [52], [54], [55]. This approach was first demonstrated in 2006, when Takahashi and Yamanaka successfully reprogrammed mouse fibroblasts into a pluripotent state, resulting in cells that closely mirrored the differentiation potential of ESCs [55], [56]. A year later, the same reprogramming strategy was applied to human fibroblasts, leading to the generation of the first human induced pluripotent stem cell (hiPSC) line [55], [57]. Importantly, iPSCs also overcome the limitations of primary cell cultures, offering an accessible and renewable source of otherwise hard-to-obtain cell types (such as neurons, CMs, and retinal cells) without the constraints of finite proliferative capacity [55], [58].

Therefore, hiPSCs have emerged as invaluable tools for modeling human development and disease. Development can be effectively modeled through the controlled differentiation of hiPSCs, a process that recapitulates key events of embryogenesis [55]. Additionally, hiPSCs are particularly well-suited for *in vitro* disease modeling [55]. Disease models can be developed by reprogramming patient-derived somatic cells into hiPSCs carrying a disease-relevant genetic background and differentiating them into the affected cell types [55]. Additionally, these models can be established by exposing healthy hiPSC-derived cells to compounds or environmental stressors that induce pathological phenotypes [55]. For instance, age-related neurodegenerative conditions can be mimicked using mitochondrial electron transfer disruptors to induce cellular senescence [55]. These approaches enable the development of *in vitro* models that recapitulate disease-specific phenotypes, which may not be accurately represented in animal models, and serve as platforms for drug screening [55].

1.3.2 *In vitro* cardiac models

Progress in *in vitro* cardiac models has been relatively slow, largely due to the complex structure and function of the native heart, an organ that comprises four distinct chambers and a diversity of cell types – including CMs, CFs, and endothelial cells (ECs) – whose coordinated interactions are essential for proper heart development and function [59], [60].

The advent of iPSC technology and the ability to direct their cardiogenic differentiation have contributed to cardiac *in vitro* research by providing an unlimited source of CMs, a cell type that is otherwise difficult to obtain [61]. iPSC-derived CMs are typically cultured in two-dimensional (2D) systems, where they grow as a monolayer on a flat surface [45], [59]. Co-culture with additional cardiac cell types, such as CFs and ECs, has been reported to support CM maturation [62]. The reproducibility and affordability of these systems have established them as suitable for high-throughput applications, exemplified by a study testing novel anti-fibrotic compounds in human CFs [45], [63]. Moreover, 2D hiPSC-derived cardiac models have been applied to disease modeling, such as in congenital heart disease, where they enabled the study of DAND5 function on human CM proliferation and differentiation [64]. Despite these advantages, 2D systems remain limited in their ability to model cardiac development and disease [59]. They fail to accurately reproduce cellular *in vivo* characteristics, since 2D attachment causes cells to alter their morphology and impede essential key cell-cell and cell-ECM interactions, on which morphogenetic and (patho)physiological processes depend [59], [65].

To address these limitations, cardiac models have evolved towards three-dimensional (3D) culture systems, which offer greater complexity and more accurately represent the native heart's structure and function [59]. These models typically consist of multiple cardiac cell types and may be assembled either with or without biological scaffolds. Examples include engineered heart tissues, spheroids, and cardiac organoids – **Figure 6** [59].

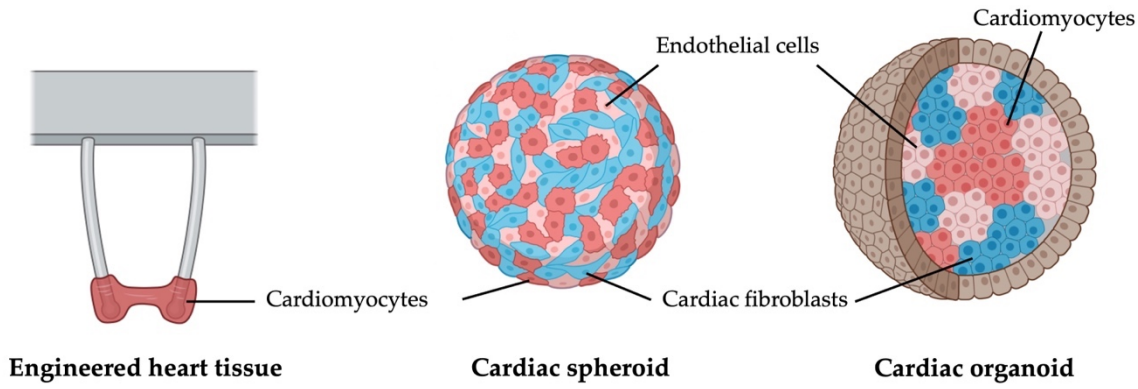

Figure 6: 3D *in vitro* cardiac models. Engineered heart tissues are generated by embedding pre-differentiated cardiomyocytes (red) within an extracellular matrix (ECM)-containing cavity or mold. Cardiac spheroids are obtained by assembling pre-differentiated cardiac cells, such as cardiomyocytes, cardiac fibroblasts (blue), and endothelial

cells (pink) in proportions that approximate the cellular composition of the heart. Cardiac organoids are formed through the aggregation of human pluripotent stem cells (hPSCs), followed by their self-organization and differentiation into multiple cardiac cell types within a 3D environment, resulting in complex structures that resemble the architecture of the native heart. Created with Biorender.

Engineered heart tissues are primarily composed of differentiated CMs, optionally incorporating CFs and ECs, often derived from hPSCs. These cells are aggregated within an ECM-containing cavity or mold to form contractile, adult-like tissue constructs [59], [66]. Cardiac spheroids are formed by culturing differentiated cardiac cells, frequently hPSC-derived, in ratios that resemble the cellular composition of the heart [59], [67]. In contrast, cardiac organoids, also referred to as cardioids, are complex hPSC-based 3D structures that self-organize and differentiate within a 3D environment, generating multiple cardiac cell types arranged in a tissue-like architecture [59], [68].

1.3.2.1 Cardiac organoids

Organoids stand out as one of the most popular 3D models. They are derived from stem cells, which, when cultured under appropriate 3D conditions, aggregate, self-organize, and differentiate into miniature organ-like structures [65]. Organoids exhibit self-renewal capacity and consist of multiple cell types arranged in a spatial configuration that partially mirrors that of the corresponding *in vivo* organ [55], [65]. Additionally, they are capable of simulating limited aspects of the organ's physiological function, such as the spontaneous contractile activity observed in cardiac organoids [65], [69]. A wide range of organoid models has been developed to date, including those representing the lung, liver, gut, kidney, brain, retina, and heart [70]. These models hold considerable potential, although some challenges remain, including incomplete cellular complexity, lack of blood perfusion and systemic integration, and high intra-batch and batch-to-batch variability [71], [72], [73].

Since 2021, an increasing number of human cardiac organoid models have been established, displaying advanced structural and functional characteristics – **Figure 7** [59]. Their development relies on the manipulation of key signaling pathways involved in cardiogenesis *in vivo* (e.g., Wnt signaling), achieved by the time-controlled exposure of hPSCs to developmental cues that direct their differentiation into cardiac lineages [59], [74]. A notable example is the work of Lewis-Israeli *et al.* [69], whose approach generates cardioids that recapitulate important stages of heart development throughout differentiation. The resulting structures closely resemble fetal heart tissue, featuring well-organized multilineage cardiac cell populations, internal chambers, and complex vessel-like structures. These organoids were further used to model the effects of pregestational diabetes on the developing heart, highlighting the utility of this system to study human diseases affecting the fetal heart [69], [74]. Meier *et al.* [75] developed epicardioids that recapitulate human LV patterning by organizing into

myocardium, including a compact subepicardial layer, and epicardium. These organoids replicate key functions of the embryonic epicardium, such as providing progenitor cells for various cardiac lineages and supporting myocardial compaction and maturation by releasing paracrine mediators. Furthermore, the authors demonstrated that their epicardioids serve as a relevant model for studying not only cardiac development but also cardiac pathological remodeling, as evidenced by the successful modulation of both congenital and stress-induced LV hypertrophy and fibrosis [75], [76]. Recently, Song *et al.* [77] generated cardioids containing the main cardiac cell types and vessel-like structures, capturing key features of the human adult heart. The cardioids were used to model acute myocardial infarction, and when subjected to ischemic and ischemia-reperfusion injuries, they reproduced the early responses to myocardial infarction as well as the subsequent fibrotic remodeling [77].

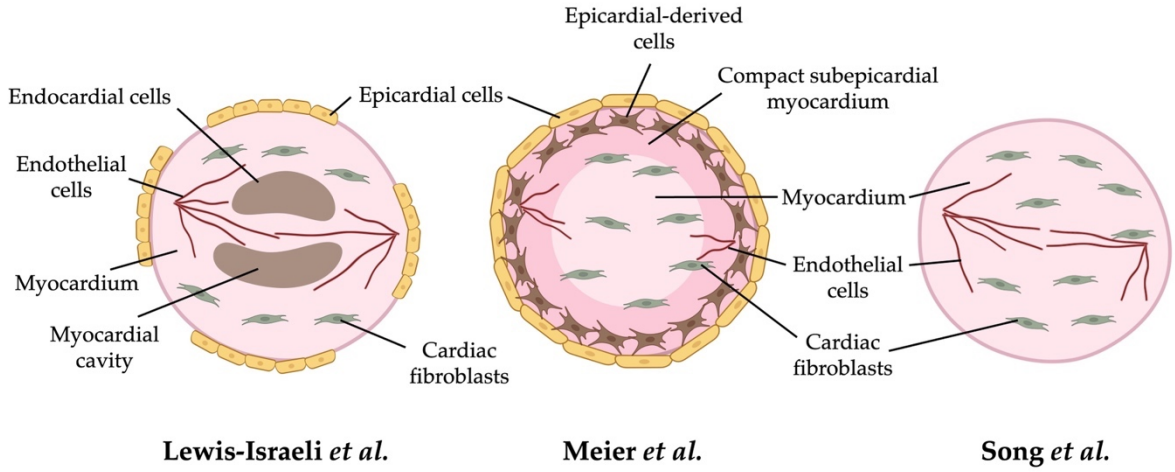

Figure 7: Advanced cardioid models. The cardioid model developed by Lewis-Israeli *et al.* includes the main cardiac cell types, including cardiomyocytes (pink), cardiac fibroblasts (green), and endothelial cells (red). It also includes an epicardial cell population, endocardial cell-lined myocardial cavities, and a complex vessel-like network. The epicardioid model described by Meier *et al.* features an outer epicardial layer and epicardial-derived cells that act as progenitors for multiple cardiac lineages. In addition, it exhibits a compact subepicardial myocardial layer (dark pink). The model reported by Song *et al*. comprises the main cardiac cell types and features a well-developed vasculature. Created with Biorender.

Given their high degree of cellular complexity, the cellular interactions they sustain, and their ability to reproduce key cardiac features, such as vessel-like networks and myocardial cavities, these advanced cardioid models represent invaluable platforms for studying both cardiac development and disease [59], [69], [75], [77].

1.4 Objectives

HFpEF is a syndrome associated with high mortality and hospitalization rates. Models that enable the identification of therapeutic targets and the development of effective therapies remain limited, with the most widely used being animal models. In this work, we aim to contribute to the establishment of a reliable human cell-based HFpEF model through the use of hiPSC-derived cardiac organoids to study the role of miRNAs in HFpEF pathophysiology. Previously in our laboratory, the hsa-miR-25-3p and hsa-miR-26a-5p miRNAs were identified as upregulated in HFpEF patients, with their mRNA targets being potentially involved in cardiac remodeling. Since fibrosis represents a key underlying mechanism of the syndrome, we hypothesize that the delivery of these miRNAs into cardioids induces fibrotic remodeling, potentially through the downregulation of their target genes *HAPLN1* and *NPPB*. Accordingly, the specific objectives of this study are as follows:

1) To generate three-dimensional human cardioids derived from hiPSCs.
2) To evaluate the responsiveness of this cardioid model to fibrosis-related stimuli and to validate markers of fibroblast activation and collagen deposition, both of which are fibrosis-associated processes.
3) To optimize miRNA delivery into cardioids by testing both liposomal- and electroporation-based approaches.
4) To investigate the effects of miRNA delivery on the expression of the target genes *HAPLN1* and *NPPB*, as well as on fibrosis-associated processes.

By examining whether the delivery of these HFpEF-related miRNAs contributes to fibrosis in cardioids, this work seeks to advance the establishment of an HFpEF *in vitro* model capable of recapitulating essential features of the syndrome.

2

MATERIALS AND METHODS

2.1. Cell culture

2.1.1. Cell line

This study utilized the commercial healthy hiPSC line WTC, registered under the Human Pluripotent Stem Cell Registry with the identifier UCSFi001-A. Its use for cardiac differentiation was approved under MTA (#GIN0006295).

2.1.2. hiPSC culture, maintenance, and storage

6-well plates were pre-coated with Geltrex (Gibco, A1569601) diluted in Dulbecco's Modified Eagle's Medium/Nutrient Mixture F-12 (DMEM/F12, Gibco, 11320-033), and incubated under standard culture conditions (37 °C, 5% CO_2) for a minimum of 60 minutes before being used for culture.

Cryopreserved cell aliquots stored at -150 °C were rapidly thawed in a 37 °C water bath. The thawed suspension was transferred dropwise to a 15 mL conical tube containing 4.5 mL of Essential 8 Flex medium (E8, Gibco, A28585-01) at room temperature (RT). Cells were centrifuged at 180 x *g* for 5 minutes at RT. The supernatant was discarded, and the cell pellet was gently resuspended in E8 supplemented with the ROCK inhibitor RevitaCell™ (Gibco, A2644501). Cells were seeded into the pre-coated 6-well plates and maintained under standard culture conditions. The following day, the medium was replaced with fresh E8 medium (without RevitaCell) and changed daily thereafter.

Cells were passaged at 70-80% confluence. Maintenance medium was aspirated, and cells were rinsed in 3 mL of Dulbecco's Phosphate Buffered Saline (DPBS, Gibco, 14190-250) pre-warmed to 37 °C and incubated for 3 minutes. Following DPBS removal, 1 mL of Versene

(Gibco, 15040-066), also pre-warmed to 37 °C, was added, and cells were incubated for 3 minutes to promote detachment. Once cells were detached, 4 mL of RT E8 medium was added to inactivate Versene, the cell suspension was transferred to a 15 mL conical tube, and centrifuged at 180 x *g* for 5 minutes at RT. The supernatant was discarded, and the cell pellet was resuspended in E8 medium supplemented with RevitaCell at RT. Cells were replated onto Geltrex-coated 6-well plates at an appropriate dilution (1:5 to 1:10). The following day, the medium was replaced with fresh E8 and changed daily thereafter.

For long-term cryopreservation, the maintenance medium was aspirated, and cells were rinsed in 3 mL of DPBS pre-warmed to 37 °C and incubated for 3 minutes. After removal of DPBS, 1 mL of Versene pre-warmed to 37 °C was added, and cells were incubated for 3 minutes. Once cells were detached, 4 mL of RT E8 was added. The resulting cell suspension was transferred to a 15 mL conical tube and centrifuged at 180 x *g* for 5 minutes at RT. Following removal of the supernatant, the cell pellet was resuspended in CryoStor CS10 cell cryopreservation medium (Sigma-Aldrich, C2874). The cell suspension was aliquoted into cryovials (Sarstedt, 72.380.005) and subjected to controlled-rate freezing to -80 °C overnight. The following day, the cryovials were transferred to -150 °C for long-term storage.

2.1.3. Generation of hiPSC-derived cardioids

Cardioids were generated using the hiPSC line WTC based on a previously published protocol [77].

In this experiment, days denoted with negative numbers refer to days preceding mesodermal induction, while day 0 and subsequent positive days correspond to successive stages of the differentiation protocol. Culture media used during differentiation were E8 and RPMI Medium 1640 (Gibco, 11875-093), supplemented either with B27 without insulin (RB-, Gibco, A18956-01) or with B27 without vitamin A (RB without vitamin A, Gibco, 12587-010).

Cells were cultured in 6-well plates until reaching approximately 70% confluence. On day -2 of differentiation, the maintenance medium was removed, and cells were rinsed in 3 mL of DPBS, pre-warmed to 37 °C, and incubated for 3 minutes. Following DPBS removal, 0.5 mL Accutase (Gibco, A11105-01) at RT was added, and cells were incubated for 5 minutes to promote detachment. Following complete cell detachment into a single-cell suspension, 4.5 mL of RT E8 medium was added to inactivate Accutase. The cell suspension was transferred to a 15 mL conical tube and centrifuged at 180 x *g* for 5 minutes at RT. Simultaneously, cell counting was performed using a Neubauer chamber. The supernatant was discarded, and the cell pellet was resuspended in 5 mL of RT E8 medium. The required volume of the cell suspension was transferred to a separate conical tube and centrifuged at 180 x *g* for 5 minutes at RT. The supernatant was discarded, and the cell pellet was resuspended in RT E8 medium

supplemented with RevitaCell. Cells were seeded in a round-bottom ultra-low attachment 96-well plate (faCellitate, F202003), at a volume of 100 μL/well. The plate was centrifuged at 100 x *g* for 3 minutes at RT and incubated at standard culture conditions. On day -1, RT E8 was renewed. On day 0, the culture medium was replaced with fresh RB-, pre-warmed to 37 °C, containing CHIR99021. On day 1, the culture medium was replaced with fresh RB-, pre-warmed to 37 °C. On day 2, the culture medium was replaced with fresh RB-, pre-warmed to 37 °C, containing IWP4. On days 4, 6, and 8, the culture medium was replaced with fresh RB- pre-warmed to 37 °C, containing Bone morphogenic protein 4 (BMP4), fibroblast growth factor (FGF), and vascular endothelial growth factor (VEGF). From day 10 to day 26, cardioids were maintained in RB without vitamin A medium, pre-warmed to 37 °C. Every 48 hours, the medium was replaced with fresh and RB without vitamin A, pre-warmed to 37ºC.

2.1.4. TGF-β treatment

Cardioids were treated with TGF-β (Bio-Techne, 240-B-002) for 11 days. On day 16 of differentiation, the culture medium was replaced with RB without vitamin A, pre-warmed to 37 °C, containing 15 ng/mL of TGF-β, resulting in final concentrations per-well of 10 ng/mL. Medium was replaced every 3 days with RB without vitamin A, pre-warmed to 37ºC, and containing TGF-β, corresponding to days 19 and 22 of differentiation. Cardioids were maintained in this medium from day 22 until the end of the differentiation protocol (day 26).

2.1.5. miRNA delivery into cardioids

2.1.5.1. Liposomal-based delivery

miRNA delivery into cardioids was performed using the Lipofectamine 3000 Transfection Reagent (Thermo Fisher Scientific, L3000008), following the manufacturer's instructions. The protocol was first optimized using cardioids on day 20 of differentiation (two cardioids per condition), by testing different miRNA and fetal bovine serum (FBS, Sigma-Aldrich, F7524) concentrations, as well as different timings of FBS addition (conditions detailed in **Table 1**).

Briefly, 0.2 μL of Lipofectamine was diluted in 5 μL of Opti-MEM medium (Thermo Fisher Scientific, 31985-070) and mixed by pipetting. The Cy3-labeled miRNA (Thermo Fisher Scientific, AM17120) was diluted in 5 μL of Opti-MEM to final concentrations of 1 μM, 100 nM, and 100 pM. The transfection mixture was prepared by mixing 5 μL of diluted Lipofectamine with 5 μL of diluted miRNA, followed by incubation at RT for 15 minutes. The RB without vitamin A medium was removed from the wells containing the cardioids, and 80 μL of Opti-MEM was added to each well. The transfection mixture was then transferred evenly

throughout the well. FBS was either included directly in the transfection mixture before incubation and addition to the wells, or added separately to the wells immediately after the incubated transfection mixture was added. In both cases, the final concentration of FBS in the well was 10%. Cardioids were maintained in the transfection medium for 5 days, after which it was replaced with RB medium without vitamin A (day 25 of differentiation). Fluorescence was assessed 2 days after delivery (day 22 of differentiation) for all the conditions, using cardioids in the 96-well plates. Six days post-delivery (day 26 of differentiation), fluorescence was assessed on cryosections (detailed in section 2.2) only for the condition with 1 μM miRNA and 10% FBS added separately to the well containing Opti-MEM and the transfection mixture.

Table 1: Conditions tested during miRNA delivery optimization.

FBS concentration	FBS addition time	Cy3-labeled miRNA concentration		
0%	-	1 μM	100 nM	100 pM
10%	Added to the transfection mixture before incubation	1 μM	100 nM	100 pM
	Added to the well containing Opti-MEM and the incubated transfection mixture	1 μM	100 nM	100 pM

Following protocol optimization, deliveries were carried out either on day 20 or on both days 11 and 20 of differentiation (two deliveries per organoid). Optimized delivery conditions consist of a miRNA concentration of 1 μM and 10% FBS added separately to the well containing Opti-MEM and the transfection mixture. Precursors of miRNA molecules potentially relevant for HFpEF were delivered into cardioids, namely pre-hsa-miR-25-3p (Thermo Fisher Scientific, PM10584) and pre-hsa-miR-26a-5p (Thermo Fisher Scientific, PM10249), with their corresponding mature sequences listed in Appendix, **Table A1**. The Cy3-labeled miRNA was used as a delivery control. Cardioids were maintained in the transfection medium for 5 days, after which it was replaced with RB medium without vitamin A (day 25 or days 16 and 25 of differentiation).

2.1.5.2. Electroporation-based delivery

Cardioids on day 20 of differentiation were carefully removed from the 96-well plate and transferred to a cuvette (four cardioids per condition) containing Cy3-labeled miRNA diluted in DPBS to final concentrations of 1 μM or 100 nM, in a total volume of 400 μL. Electroporation was performed using an electroporator (BTX Safety Stand 630B), according to the

settings listed in **Table 2**. The culture medium in the original wells was replaced with 180 μL or 200 μL of Opti-MEM supplemented with RevitaCell, depending on the addition of FBS. The electroporated cardioids were then gently returned to their respective wells. Following cardioid transfer, in the wells with 180 μL of Opti-MEM, 20 μL of FBS was added, resulting in a final concentration of 10% FBS, whereas in the other wells already containing 200 μL of medium, FBS was not added. Two days after electroporation (day 22 of differentiation), fluorescence was assessed using cardioids in the 96-well plates.

Table 2: Electroporation settings for miRNA delivery into cardioids.

	Poring pulse	**Transfer pulse**
Voltage	175 V	20 V
Pulse length	5 ms	50 ms
Interval	100 ms	50 ms
Number of pulses	2	5

2.2. Cardioid embedding and cryosectioning

On day 26 of differentiation, cardioids were transferred to 1.5 mL tubes. After removal of the residual culture medium, cardioids were rinsed in phosphate-buffered saline (PBS). Fixation was performed with 4% paraformaldehyde (PFA) for 40 minutes at RT. Following an additional wash with PBS, cardioids were dehydrated in a 20% sucrose solution (1x PBS; 20% sucrose (BioChemika, 84099); 0.01% sodium azide (NaN_3, Merck, 1.06688.0100)) at 4 °C until they gradually descended to the bottom of the tube. The solution was replaced with 30% sucrose (1x PBS; 20% sucrose; 0.01% NaN_3), and cardioids were maintained at 4 °C. Once cardioids had sunk to the bottom of the tube, they were transferred to Cryomold Intermediate cryomolds (Tissue-Tek, 4566), and the remaining sucrose solution was carefully removed. Cardioids were embedded in OCT Mounting media (VWR Chemicals, 361603E) and positioned at the center of the mold. After resting for 40 minutes at RT, the molds were placed in dry ice for 15 minutes and then stored at -80 °C .

OCT-embedded blocks were sectioned at a thickness of 12 μm using a Leica CM3050 S cryostat (Leica Biosystems), and sections were mounted onto Superfrost Plus Adhesion Microscope Slides (Epredia, J1800AMNZ). After a 30-minute drying period at RT, slides were stored at -4°C.

2.3. Staining

2.3.1. Immunostaining

2.3.1.1. Cryosections

Cryosections were rinsed twice in PBS-Triton (1x PBS, 0.5% Triton X-100 (Sigma-Aldrich, T8787)) for 5 minutes each and then incubated with blocking solution (BS, 1x PBS, 0.5% Triton X-100, 2% Bovine Serum Albumin (BSA, NZY Tech, MB04602), 5% Donkey Serum (DS, Sigma-Aldrich, D9663)) for a minimum of 1 hour at RT, covered with a parafilm strip. Primary antibodies (detailed in Appendix, **Table A2**) were diluted in the same BS, and cryosections were incubated with this solution overnight at 4 °C in a humidified chamber, covered with a parafilm strip. The following day, cryosections were rinsed three times in PBS-Triton for 5 minutes each. Secondary antibodies (detailed in Appendix, **Table A2**) were diluted in BS, and cryosections were incubated with this solution for 2 hours at 4°C in a humidified chamber, covered with a parafilm strip. Cryosections were rinsed twice in PBS-Triton for 5 minutes each, followed by a rinse in 1x PBS for 5 minutes. Cryosections were incubated with 4',6-diamidino-2-phenylindole (DAPI, 1:100 diluted in BS without DS) for 15 minutes at RT in the dark, followed by two rinses in PBS for 5 minutes each. Cryosections were mounted using Mowiol Mounting Medium, covered with a coverslip (Menzel Glaser), and left to dry at RT for 30 minutes. Once dry, coverslip edges were sealed with clear nail polish, and samples were stored at 4 °C.

2.3.1.2. Whole-mount

Cardioids on day 26 of differentiation were collected into 1.5 mL tubes, the remaining medium was removed, and cardioids were rinsed in PBS. Fixation was performed with 4% PFA for 40 minutes at RT under gentle agitation. Subsequently, cardioids were rinsed three times with PBS for 10 minutes each and incubated with BS overnight at 4 °C. The following day, cardioids were rinsed three times with PBS for 1 hour each, and then incubated overnight at 4 °C with primary antibodies (detailed in Appendix, **Table A2**) diluted in BS. After three rinses with PBS, for 1 hour each, cardioids were incubated overnight at 4 °C with secondary antibodies (detailed in Appendix, **Table A2**) diluted in BS, and were protected from the light from this step onward. Cardioids were rinsed again three times with PBS, for 1 hour each, and incubated with DAPI (1:100 diluted in BS without DS) for 15 minutes. Cardioids were rinsed three times with PBS, the first two for 1 hour each and the last one overnight. Subsequently, they were positioned between small coverslips, sealed with a larger coverslip, and mounted using RapiClear 1.49 solution (SUNJinLab, RC149001). All rinsing and incubation steps were carried out under gentle agitation.

2.3.2. Masson's Trichrome Staining

Cryosections were rinsed in PBS 1x for 1 minute and incubated with Bouin's solution (VWR Chemicals, 7000.1000) at 60 °C for 30 minutes. The fixative was then removed by thoroughly washing the slides under running tap water for 5 minutes. Subsequently, cryosections were incubated with Weigert's iron hematoxylin (Merck Millipore, 1.15973.0002) for 10 minutes to stain cell nuclei, rinsed under running water for 5 minutes, and then washed in distilled water. Cryosections were incubated for 7 minutes with Biebrich Scarlet-Acid Fuchsin solution, prepared by mixing 90 mL of Biebrich Scarlet's 1% (Atom Scientific, RRBD16079-W) in distilled water, 10 mL of acid fuchsin 1% (Merck Millipore, 1.05231.0025) in distilled water, and 1 mL of glacial acetic acid (Merck Millipore, CAS 64-19-7) to stain cell's cytoplasm. Sections were rinsed in distilled water and differentiated in phosphomolybdic acid (Bio-Optica, 05-M05003) for 15 minutes under microscopic control. Subsequently, collagen fibers were stained with 2% Aniline Blue solution (Sigma-Aldrich, 1003278858) in glacial acetic acid for 15 minutes, followed by a rinse in distilled water. Cryosections were then dehydrated sequentially in 70%, 96%, and 99.9% ethanol (AGA) for 1 minute each under gentle agitation, cleared in xylene (VWR Chemicals, 1.08298.4000) for 15 minutes, and mounted with Histofluid Mounting Medium (Marienfeld Superior, 6900002). Coverslips (VWR Chemicals, ECN 631-1575) were applied, and slides were left to dry for at least 1 hour at RT before storage at RT.

2.4. Microscopy

Brightfield images of cardioids during the differentiation protocol were acquired on an EVOS XL Core system, using a 4x / 0.13 NA objective.

For immunostained cryosections, images were acquired on a Zeiss LSM710 system using 10x /0.3 NA, 40x /1.2 NA water immersion, and 63x / 1.4 NA oil immersion objectives with ZEN Black 2011 SP1 software. Whole-mount staining images were acquired on a Zeiss Apotome 3 Plus system, using a 40x /1.2 NA water immersion objective.

Brightfield and fluorescence images of cardioids in 96-well plates, 2 days after miRNA delivery, were acquired on a Zeiss Axiovert 40 CFL system, using a 10x/0.25 NA objective with a ZEN 2.6 (blue edition) software. Confocal fluorescence images of organoid cryosections, 6 days after lipofectamine-based miRNA delivery, were acquired on a Zeiss LSM710 system, using a 20x/0.8 NA objective with ZEN Black 2011 SP1 software.

Brightfield images of Masson's Trichrome-stained cryosections were acquired on a Zeiss Imager Z2 system equipped with a Zeiss Axiocam 506 mono [Zeiss Axiocam 105 color], using a 10x/ 0.3 NA objective with ZEN Blue 2012 software.

2.5. Gene expression analysis

2.5.1. RNA extraction

8 to 11 cardioids on day 26 of differentiation were collected into 1.5 mL tubes, and the culture medium was carefully removed. Cardioids were mechanically disrupted using a tissue grinder. 300 μL of TRI Reagent (Sigma-Aldrich, 102326229) was added to the tube, and cardioids were further dissociated by vigorous pipetting to ensure complete homogenization. RNA was extracted using the Direct-Zol RNA MiniPrep Kit (Zymo Research, R2052), following the manufacturer's instructions.

RNA concentration and purity were assessed using a Nanodrop 2000 spectrophotometer (Thermo Fisher Scientific). RNA samples were stored at -80 °C for complementary deoxyribonucleic acid (cDNA) synthesis and downstream transcriptomic analyses.

2.5.2. cDNA synthesis

cDNA synthesis was performed using the RevertAid RT Kit (Thermo Fisher Scientific, K1691), according to the manufacturer's instructions.

Briefly, the volume corresponding to 1000 ng of RNA was mixed with 1 μL of Oligo$(dT)_{18}$ primer and nuclease-free water (Ambion, AM9937), to a final volume of 12.5 μL. The mixture was incubated at 65 °C for 5 minutes in a thermal cycler (MyCycler™ Thermal Cycler, Bio-Rad). During this step, a master mix was prepared containing, per sample, 4 μL of 5x Reaction Buffer, 0.5 μL of RiboLock RNAse Inhibitor, 2 μL of deoxyribonucleotides, and 1 μL of RevertAid Reverse Transcriptase. Following the initial incubation, 7.5 μL of the master mix was added to each sample, and reverse transcription reaction was performed by incubating the mixture at 42 °C for 60 minutes, followed by enzyme inactivation at 70°C for 5 minutes. The resulting cDNA was diluted 1:10 by adding 180 μL of nuclease-free water and stored at -20 °C.

2.5.3. RT-qPCR

Real-time quantitative polymerase chain reaction (RT-qPCR) was performed using the SensiFAST SYBR Lo-ROX Kit (Bioline, BIO-94020), following the manufacturer's instructions.

Each reaction mixture contained 2 μL of cDNA (previously diluted 1:10), 10 μL of SensiFAST SYBR Lo-ROX Mix, 0.8 μL each of forward and reverse primers at a concentration of 10 μM (primer sequences provided in Appendix, **Table A3**), and 6.4 μL of nuclease-free water, resulting in a final volume of 20 μL. Amplification and fluorescence quantification were performed using a QuantStudio 5 Real-Time PCR System (Thermo Fisher Scientific), according to the cycling conditions outlined in **Table 3**.

Table 3: Thermal cycling conditions used for RT-qPCR.

Step	Temperature (°C)	Duration	Cycles
Polymerase activation	95	2 min	1
PCR	95	5 sec	40
	Specific for each primer (Appendix, **Table A3**)	15 sec	
	72	20 sec	
Melting curve	95	1 sec	1
	60	20 sec	
	95	1 sec	

The relative expression of target genes was calculated using the $2^{-\Delta\Delta Ct}$ method, with normalization to the housekeeping gene *GAPDH* (primer sequences detailed in Appendix, **Table A3**). Each cDNA sample was analyzed in triplicate.

2.6. Quantification of α-SMA and collagen deposits

Quantification was performed using the FIJI software (ImageJ, version 1.54p). For α-SMA analysis, fluorescence image channels were split, and the DAPI channel was used to delineate (with the freehand selections tool) and measure the total organoid area. Thresholding was then applied to the α-SMA channel, using values of 1726 for the TGF-β experiment and 2965 for the miRNA delivery experiment. The threshold-restricted area was measured, normalized to the total organoid area, and expressed as a percentage.

For collagen deposition analysis, brightfield images of Masson's Trichrome staining in RGB format were used to delineate (with the freehand selections tool) and measure the total organoid area. Images were then processed using the Color Deconvolution plugin with the preset for Masson's Trichrome. The blue channel (collagen-specific) was selected, and pixel width, height values, and voxel depth information from the original image were copied into this channel. Threshold values of 95 (TGF-β experiment) and 120 (miRNA delivery experiment) were applied. The threshold-restricted area was measured, normalized to the total organoid area, and expressed as a percentage.

2.7. Statistics

Statistical analysis was performed using the GraphPad Prism version 9.5.0. Data normality was assessed with the Shapiro-Wilk test.

For the TGF-β experiment, normally distributed data from two experimental groups were compared using an unpaired t-test. The number of cardioids analyzed per condition was n=4 for α-SMA quantification and n=3 for collagen deposits quantification.

For the miRNA delivery experiment, normally distributed data from more than two experimental groups were analyzed using one-way analysis of variance (ANOVA) followed by Tukey's post hoc multiple comparisons test. For the delivery performed on day 20 of differentiation, the number of cardioids analyzed per condition was as follows: n=4 for α-SMA quantification, as well as for control and hsa-miR-26a-5p conditions in collagen deposits quantification, and n=3 for the hsa-miR-25-3p and hsa-miR-25-3p + hsa-miR-26a-5p conditions in collagen deposits quantification. For delivery on both days 11 and 20 of differentiation, n=3 for α-SMA quantification, as well as for hsa-miR-25-3p and hsa-miR-25-3p + hsa-miR-26a-5p conditions in collagen deposits quantification, and n=4 for the control and hsa-miR-26a-5p conditions in collagen deposits quantification.

A p-value < 0.05 was considered statistically significant. Results are presented in column plots displaying the mean ± standard deviation (SD).

3

RESULTS AND DISCUSSION

3.1. Generation of hiPSC-derived cardioids

In the context of cardiac *in vitro* research, hPSC-derived models have predominantly relied on 2D systems focused on CM differentiation [78]. Although certain approaches incorporated additional cardiac cell types, such as ECs and CFs, these systems remained limited in their ability to reproduce the 3D cellular interactions that characterize the physiological cardiac microenvironment and are essential for cardiac function [59], [60], [62]. In response, 3D cardiac models have been introduced, with cardioids emerging as a particularly promising approach, as hPSCs self-organize and differentiate into the major cardiac cell types within a 3D context, more faithfully recapitulating structural and functional characteristics of the native heart [59].

In this study, we generated hiPSC-derived cardioids that recapitulate key structural and functional features of the native heart, including spontaneous contractile activity, the presence of major cardiac cell types, and the formation of complex vessel-like structures (**Figure 8**). The differentiation protocol was developed based on a previously published approach [77] (**Figure 8A**). Here, mesoderm and cardiogenic mesoderm induction was achieved through the time-dependent modulation of the Wnt signaling pathway. Wnt signaling was first activated on day 0, using the canonical pathway activator CHIR99021, and subsequently inhibited on day 2 by the addition of IWP4, a Wnt pathway inhibitor (**Figure 8A**) [69]. Between days 4 and 10, cell fate specification into CMs, ECs, and CFs was promoted by the addition of FGF, VEGF, and BMP4 (**Figure 8A**) [77]. From days 10 to 26, while maintained in RB without vitamin A medium, these cells matured as a result of intercellular communication and coordinated cellular rearrangements, exemplified by the formation of vessel-like structures, ultimately giving rise to a complex heart-like tissue (**Figure 8**) [79], [80].

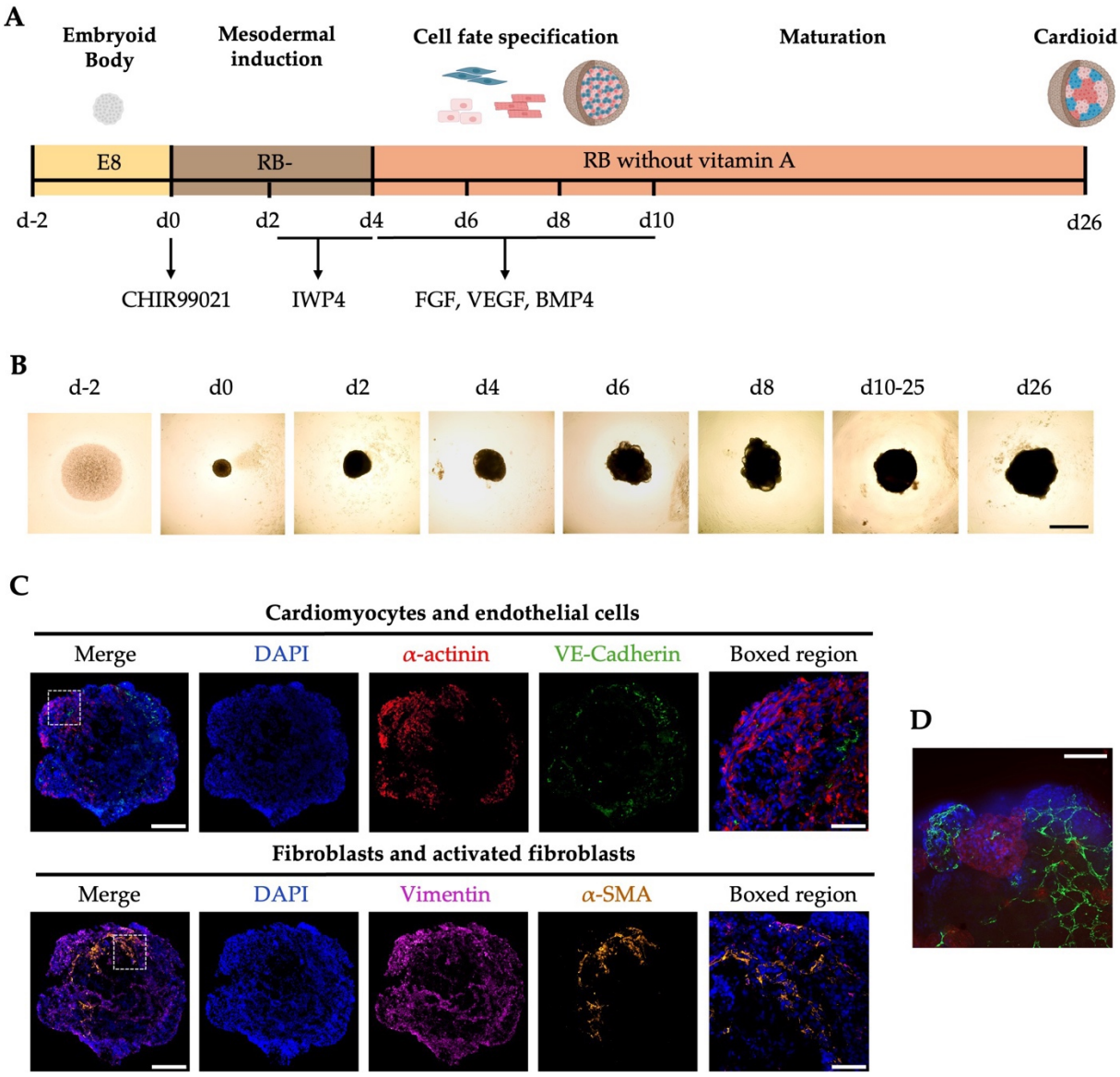

Figure 8: **Generation of hiPSC-derived cardioids**. **A**. Schematic overview of the differentiation protocol used to generate human cardioids using human induced pluripotent stem cells (hiPSCs), based on a previously published protocol [77]. **B.** Brightfield images of cardioids throughout the differentiation protocol. Scale bar = 1 mm. **C.** Immunostaining of cardioid cryosections on day 26 of differentiation, showing cardiomyocytes (α-actinin, red), endothelial cells (vascular endothelial cadherin (VE-Cadherin), green), fibroblasts (Vimentin, magenta), and activated fibroblasts (α-smooth muscle actinin (α-SMA), orange). Nuclei were counterstained with DAPI (blue). Boxed regions show higher-magnification images (40x) of the regions outlined by white dashed lines in the merged image (10x). Scale bar = 200 μm; boxed regions = 50 μm. **D.** Region of a whole-mount cardioid stained for α-actinin (red) and VE-Cadherin (green), showing cardiomyocytes and endothelial cells, respectively. Nuclei were counterstained with DAPI (blue). Endothelial cells are organized into complex, vessel-like structures. Scale bar = 50 μm.

Throughout this differentiation protocol, cardioids progressively increased in size, with the most pronounced expansion occurring between days 0 and 10 (**Figure 8B**). From day 10 onwards, their size remained relatively stable, showing only minor increases until the end

of the differentiation process. Formation of small cavities was observed between days 4 and 8, followed by their gradual filling in the subsequent days, with the cardioids becoming increasingly compact from day 10 onwards (**Figure 8B**). Spontaneous contractile activity was first detected at day 6, with the majority of cardioids beating by day 8. On day 10, all cardioids were beating, although beating patterns varied: some contracted as a whole, whereas others displayed beating restricted to specific regions. By the end of the differentiation, the majority of cardioids were beating as a whole, indicating a progressive CM maturation over time.

Confocal imaging of immunostained cardioid cryosections revealed the presence of key cardiac cell types – CMs, ECs, and CFs – distributed throughout the organoid, as identified by the expression of α-actinin, vascular endothelial cadherin (VE-Cadherin), and the intermediate filament protein Vimentin, respectively (**Figure 8C**) [77]. Complementary whole-mount staining of cardioids showed that the endothelial cell population was organized into complex, vessel-like structures (**Figure 8D**). Moreover, cryosection immunostaining for α-SMA, a protein upregulated during the activation of CFs into CMFs and a widely used marker of this population, revealed that a subset of vimentin-positive fibroblasts also express α-SMA, indicating their transition into an active state (**Figure 8C**) [30], [77].

Altogether, these results validate our differentiation protocol as suitable for generating cardiac organoids that reproduce essential functional and structural features of the heart, including contractile activity, the presence of the major cardiac cell types, and their organization into a tissue-like architecture, as illustrated by the formation of vessel-like networks.

3.2. Suitability of cardioids for modeling cardiac fibrosis

Fibrosis is a key pathological mechanism underlying HFpEF [9]. We therefore sought to evaluate whether our cardioid model was responsive to fibrosis-related stimuli and could thus serve as a relevant platform for modeling fibrosis-associated cardiac conditions.

For this purpose, we induced the activation of CFs into CMFs, the main cellular effectors of fibrosis, to characterize the activation process and its impact on ECM deposition in our cardioid model [19]. To this end, cardioids were treated with 10 ng/mL of TGF-β for 11 days, as this cytokine is a key driver of FMT [19]. During this process, the expression of α-SMA is promoted, making this protein a hallmark marker of myofibroblasts [19], [30]. Moreover, TGF-β stimulation promotes the production, secretion, and stabilization of ECM proteins, particularly collagen, ultimately resulting in collagen deposit formation [19], [23], [30]. Accordingly, α-SMA and collagen expression were analyzed to characterize CF activation and ECM deposition, respectively, in our cardioid model after TGF-β treatment. For that, two complementary approaches were used: immunostaining and Masson's Trichrome staining (**Figure 9**).

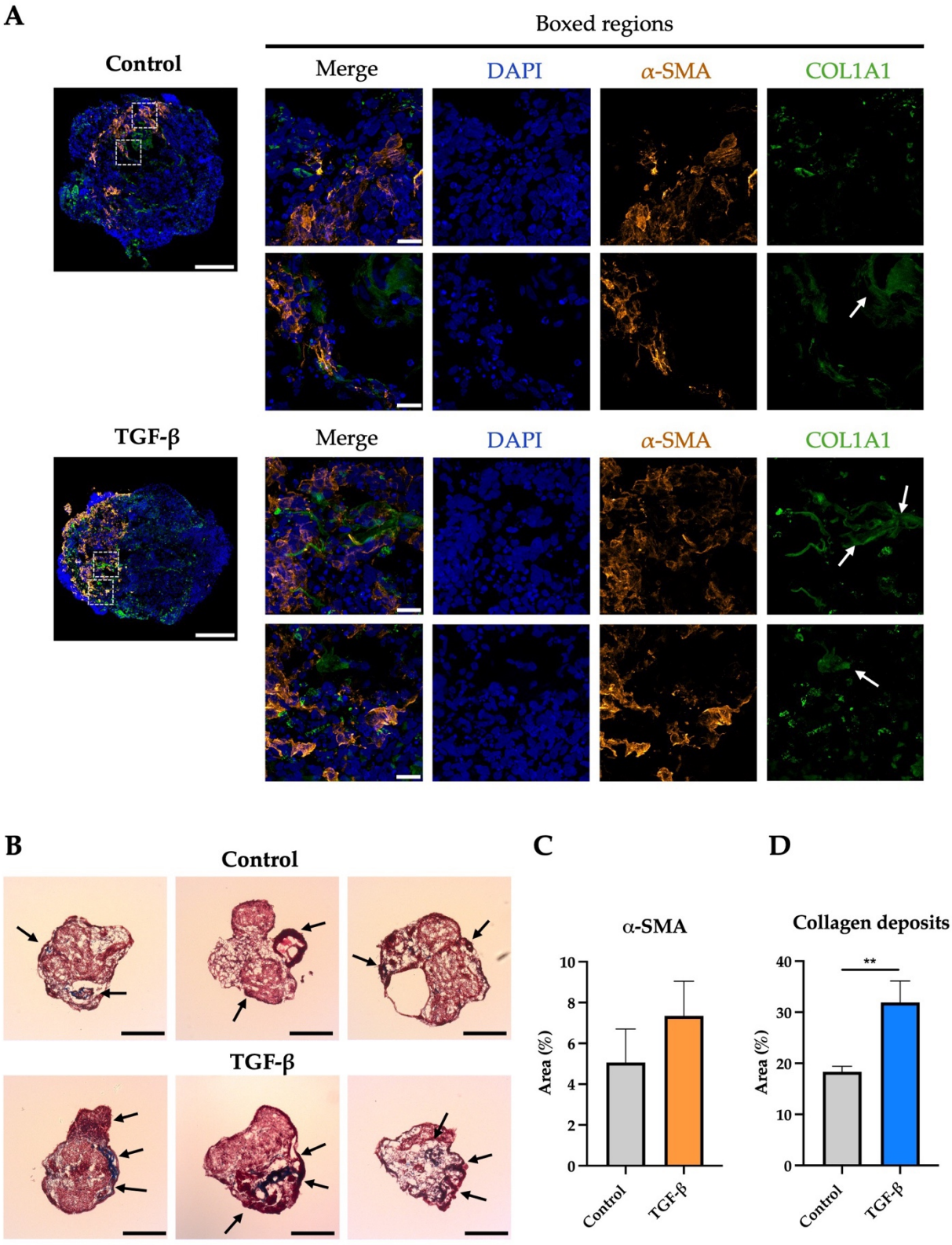

Figure 9: Characterization of α-SMA expression and collagen deposition in control and TGF-β-treated cardioids. **A.** Immunofluorescence images of cardioid cryosections, showing control (top) and Transforming Growth Factor β (TGF-β)-treated (bottom) conditions. Immunostaining shows activated fibroblasts marked with α-smooth muscle actinin (α-SMA, orange) and collagen type I alpha 1 chain (COL1A1, green). Nuclei were counterstained with DAPI

(blue). Boxed regions correspond to the areas outlined by white dashed lines on the left (10x), shown at higher magnification on the right (63x). White arrows indicate regions of meshed collagen. Scale bar = 200 μm; boxed regions = 20 μm. **B.** Masson's Trichrome staining of cardioid cryosections, showing control (top) and TGF-β-treated (bottom) conditions. Collagen fibers are stained in blue, cytoplasm in red, and nuclei in dark red. Black arrows indicate regions with evident collagen deposition. Scale bar = 500 μm. **C.** Quantification of α-SMA, normalized to total organoid area, in control (grey) and TGF-β-treated (orange) cardioids. Data are shown as mean ± SD (n=4). Comparison by unpaired t-test revealed no statistically significant differences ($p > 0.05$). **D.** Quantification of collagen deposits, normalized to total organoid area, in control (grey) and TGF-β-treated (blue) cardioids. Data are shown as mean ± SD (n=3). Comparison by unpaired t-test revealed statistically significant differences (** $p < 0.01$).

Immunostaining was performed for α-SMA and the α1 chain of type I collagen (COL1A1), the predominant collagen type in cardiac ECM *in vivo* (**Figure 9A**) [81]. The immunofluorescence images on the left show that, in control cardioids, α-SMA staining is restricted to small regions, while in TGF-β-treated cardioids it extends across a substantially larger area (**Figure 9A**). Regarding COL1A1, immunostaining shows that, under both conditions, collagen is present in two forms: as thin and sparse fibers or as dense mesh-like deposits generated by the interlacing of thinner fibers (**Figure 9A**). The higher-magnification images of the boxed regions suggest that these dense meshes, indicated by white arrows, are more pronounced in TGF-β-treated cardioids compared to controls (**Figure 9A**). This is consistent with literature reporting alterations in collagen structures following TGF-β treatment [63]. Although quantifying both thin fibers and collagen dense meshes would be of interest, the intensity threshold method used here is not suitable for this purpose, since it preferentially detects thin fibers, which typically present a stronger signal, underestimating the contribution of dense collagen meshes. A more accurate analysis would require a considerably more complex and time-consuming approach [63]. For this reason, quantitative analysis was restricted to α-SMA levels (**Figure 9C**). The results showed an increase in α-SMA expression in TGF-β-treated cardioids (**Figure 9C**). Nevertheless, the difference between control and TGF-β-treated cardioids did not reach statistical significance (**Figure 9C**). This may be attributed to high intra-batch variability as well as to the limited number of cardioids analyzed per condition (n=4) [73].

Masson's Trichrome (MT) staining is widely used for assessing fibrosis, as it differentially colors tissue components. This technique employs three dyes, with aniline blue specifically labeling collagen fibers, allowing for the identification of fibrotic deposits [82], [83]. In brightfield images of MT-stained cryosections from control and TGF-β-treated cardioids, collagen deposits, indicated by dark arrows, appear as blue regions, as well as dark red areas arising from dye overlap (**Figure 9B**). These deposits are present under both conditions, but display a greater extent and intensity in cardioids treated with TGF-β (**Figure 9B**). Quantification of collagen deposits revealed a statistically significant increase in TGF-β-treated cardioids compared with controls (**Figure 9D**).

Taken together, these results demonstrate that our cardioid model is responsive to TGF-β stimulation, with treatment promoting the activation of CFs into CMFs, as suggested by an increased α-SMA expression (**Figure 9C**) [19], [30]. The activated cells, in turn, drove excessive ECM production, secretion, and stabilization, ultimately resulting in collagen accumulation, confirmed by the statistically significant increase in collagen deposits (**Figure 9D**) [19], [23], [30]. Overall, these findings support the suitability of our cardioid model as a platform for studying fibrosis-related cardiac conditions, including HFpEF. Importantly, both α-SMA expression and, most notably, collagen deposits emerge as useful parameters for assessing CF activation and ECM accumulation in our cardioid model, providing a standard for the interpretation of fibrosis-related effects in the context of future experiments.

3.3. miRNA delivery into cardioids

A recent RNA-sequencing analysis of left ventricular myocardial biopsies from HFpEF patients identified differentially expressed mRNA and miRNA molecules and further predicted miRNA-mRNA interactions potentially implicated in the pathogenesis of the syndrome [15]. These predicted interactions were subsequently validated *in vitro* by transfecting 2D cultures of primary CMs with a subset of the upregulated miRNAs found in HFpEF samples [15]. The experiments demonstrated that hsa-miR-25-3p and hsa-miR-26a-5p downregulated the predicted target gene *HAPLN1*, whereas hsa-miR-26a-5p suppressed the expression of the *NPPB* gene [15]. Although additional miRNAs were found to downregulate these targets in the mentioned study, hsa-miR-25-3p and hsa-miR-26a-5p exerted the most pronounced downregulatory effects [15]. In the context of this work, we aimed to assess whether the observed downregulation is reproducible in our 3D cardioid model. Such interactions may underlie fundamental pathophysiological processes in HFpEF, including fibrosis, and could be important for advancing the development of a representative model of the syndrome.

To this end, the appropriate nucleic acid delivery method is crucial, with electroporation- and liposomal-based methods being among the most widely used, achieving efficiencies above 80% in 2D cultures [84]. Electroporation employs short electrical pulses to increase cell membrane permeability, thereby facilitating nucleic acid entry [85], [86]. In contrast, liposomal-based delivery relies on the formation of positively charged lipid vesicles encapsulating the genetic material. These vesicles subsequently fuse with the negatively charged cell membrane, releasing their cargo into the cell [86], [87].

However, achieving transient gene silencing in 3D structures is challenging, as organoids are dense and compact, making the delivery of the genetic material more difficult [84]. One way to address this challenge is to mechanically disrupt established organoids, followed

by the delivery of nucleic acid molecules and subsequent cell reseeding [84], [88]. This approach, however, compromises the intrinsic self-organization and tissue-like architecture of the organoid [84]. Another strategy is to transfect cells in 2D culture before transferring them into a 3D system, but this method restricts the biological questions that can be addressed [84], [89]. Given these limitations, efforts have been made to refine existing delivery methods [90]. For liposomal-based delivery, one modification involves the addition of serum, which has been shown to enhance delivery efficiency whether introduced during or after liposome-nucleic acid complex assembly. This effect is concentration-dependent, with 10% serum consistently providing the most favorable results [90]. Given this background, our approach was to optimize the miRNA delivery protocol in cardioids by testing both electroporation- and liposomal-based methods under serum and serum-free conditions, and at different miRNA concentrations (**Figure 10**). For this purpose, a Cy3-labeled miRNA mimicking endogenous mature miRNAs was used, enabling monitoring of delivery through its fluorescence.

For liposomal-based delivery, the Cy3-labeled miRNA was tested at three concentrations: 1 μM, 100 nM, and 100 pM (**Figure 10A**). Following the strategy described in the aforementioned study, in which serum was added either during or after liposome-nucleic acid complex formation [90], we assessed the effect of serum supplementation at these two stages (**Figure 10A**). Fluorescence imaging was performed two days post-delivery (day 22 of differentiation) and showed that cardioids transfected with the highest miRNA concentration, 1 μM, displayed the strongest and most homogeneous signal, indicating the highest delivery efficiency (**Figure 10A**). At 100 nM, fluorescence was weaker and rather heterogeneous, whereas at 100 pM the signal was barely detectable (**Figure 10A**). Regarding serum supplementation and its timing, the condition in which 10% FBS was added after the formation of complexes was the only one that produced detectable fluorescence even at the lowest miRNA concentration, and it appeared to enhance delivery efficiency at 1 μM, when compared to the conditions in which serum was either absent or added during complex formation (**Figure 10A**). These findings suggest that higher miRNA concentration, combined with serum supplementation after liposome-nucleic acid complex formation, enhances miRNA delivery efficiency in our cardioid model (**Figure 10A**).

For electroporation-based delivery, different concentrations of miRNA were tested (1 μM and 100 nM), and the impact of serum supplementation was also evaluated (**Figure 10B**). Fluorescence imaging performed two days after delivery (day 22 of differentiation) revealed that, in the absence of serum, both miRNA concentrations produced comparable signals, indicating similar delivery efficiency (**Figure 10B**). In contrast, the presence of serum influenced delivery depending on the miRNA concentration: it appeared to enhance uptake at 1 μM but reduce it at 100 nM, where fluorescence was undetectable (**Figure 10B**).

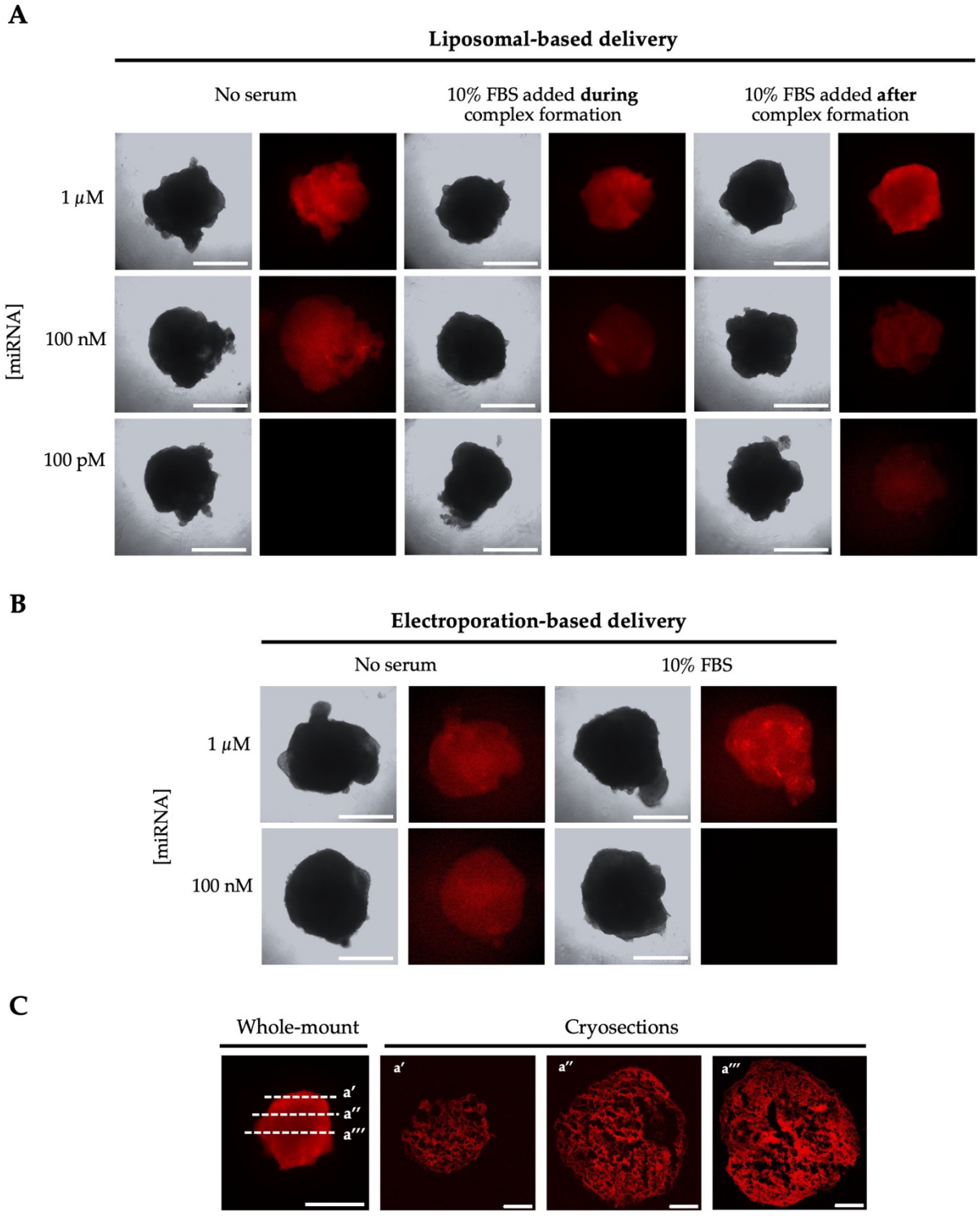

Figure 10: Optimization of miRNA delivery. A. Brightfield and fluorescence images of cardioids two days post Cy3-labeled miRNA delivery (red) using a liposomal-based approach with Lipofectamine 3000 Transfection Reagent. Different concentrations of miRNA and fetal bovine serum (FBS) were tested, as well as the timing of FBS addition. Scale bar = 1 mm. **B.** Brightfield and fluorescence images of cardioids two days post Cy3-labeled miRNA delivery (red) using electroporation-based delivery. Different miRNA and FBS concentrations were tested. Scale bar = 1 mm. **C.** Imaging of cardioid cryosections six days post liposomal-based delivery using 1 μM of Cy3-labeled

miRNA and 10% FBS added after liposomal-nucleic acid complex formation. The left panel displays the entire organoid, with the sectioning planes (a'-a''') indicated. Scale bar = 1 mm. The panels on the right (a'-a''') show fluorescence distribution across the corresponding cryosections. Scale bar = 200 μm.

When comparing both approaches, liposomal-based delivery provided greater consistency, as it remained effective across different miRNA concentrations and under both serum and serum-free conditions. Considering also that electroporation carries the risk of permanent cell damage and even cell death, we focused subsequent analyses on liposomal-based delivery, specifically the condition using 1 μM miRNA and serum supplementation after complex formation [86]. To further explore delivery efficiency under this condition, particularly concerning durability and distribution to the inner regions, a cardioid was harvested 6 days post-delivery (day 26 of differentiation) and subsequently cryosectioned (**Figure 10C**). Fluorescence was detected in cryosections across multiple planes of the organoid, with no signal reduction in deeper regions, indicating both the durability of delivery and its effectiveness in reaching the inner areas rather than being restricted to the surface of the organoid (**Figure 10C**). Accordingly, this condition was selected as optimal for HFpEF-related miRNAs delivery in the subsequent experiments.

3.4. Delivery of HFpEF-related miRNAs to cardioids

The potentially HFpEF-relevant miRNAs, hsa-miR-25-3p and hsa-miR-26a-5p, were delivered into cardioids in their precursor (non-mature) forms, using the previously optimized delivery conditions. Once internalized, they were processed by the endogenous cellular machinery into mature miRNAs, capable of binding target mRNAs and mediating gene silencing (**Figure 4**). In this context, hsa-miR-25-3p is expected to downregulate *HAPLN1* mRNA, whereas hsa-miR-26a-5p is predicted to target both *HAPLN1* and *NPPB* mRNAs, leading to their downregulation [15].

Given that these miRNAs were identified as upregulated in patients of advanced age [15], delivery was performed on day 20 of differentiation. At this stage, cardioids are already well-established and undergo minimal structural alterations, thereby representing a consolidated cardiac phenotype. Notably, Lewis-Israeli *et al.* demonstrated that *HAPLN1* and *NPPB*, two genes associated with cardiac development [15], are expressed on day 11 of differentiation and display similar expression patterns, as revealed by RNA-sequencing analysis of their cardioid model [69]. Considering the comparability of their model to ours, we additionally performed deliveries on both days 11 and 20 of differentiation to assess whether repeated administrations could produce a cumulative effect.

3.4.1. Impact of miRNA delivery on target gene expression

To determine whether the delivered miRNAs downregulated their predicted mRNA targets, as previously validated in 2D cultures of CMs, *HAPLN1* and *NPPB* levels were assessed by RT-qPCR [15]. Analyses were performed in cardioids on day 26 of differentiation, corresponding to 6 days post-delivery, from two independent batches (**Figure 11**).

The results showed an uneven downregulation of the target genes *HAPLN1* and *NPPB* across batches and experimental groups, without reaching statistical significance (**Figure 11**). In cardioids from batch 1, *HAPLN1* expression remained unchanged regardless of whether delivery was performed once on day 20 of differentiation or twice on days 11 and 20 (**Figure 11A**). A similar outcome was observed in batch 2 cardioids after a single delivery on day 20; however, when deliveries were performed on both days 11 and 20, a reduced expression of *HAPLN1* was observed, suggesting a cumulative effect of repeated deliveries (**Figure 11B**). For *NPPB*, results varied considerably between batches; however, in both cases, no reduction in gene expression was observed (**Figure 11C, D**).

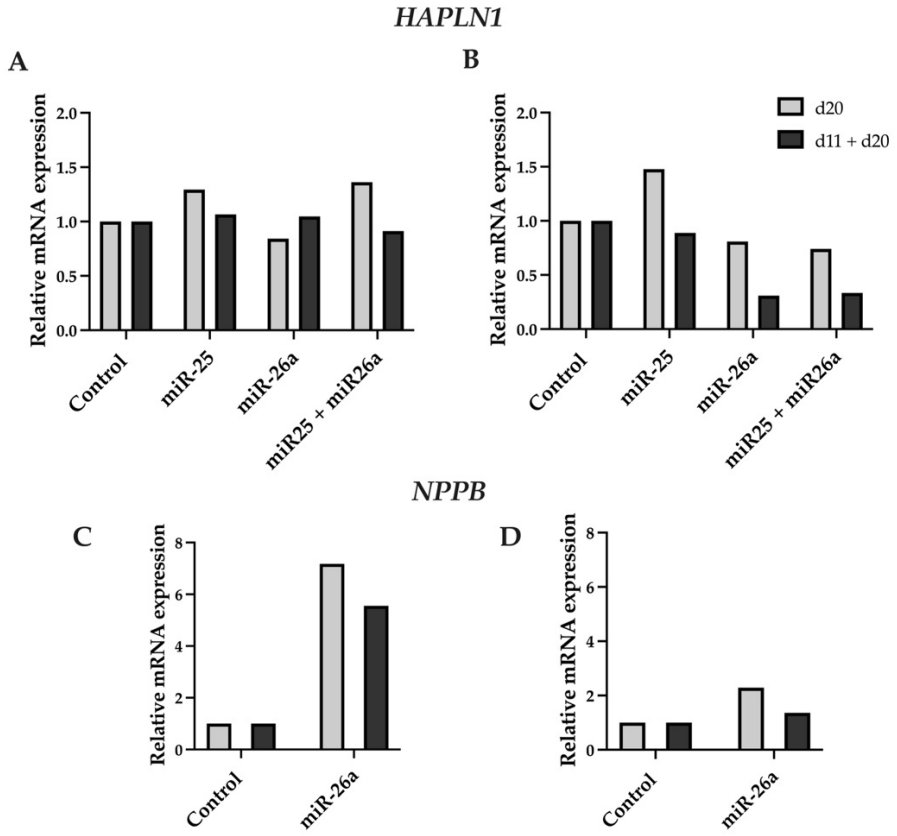

Figure 11: Evaluation of miRNA-mediated silencing of the HFpEF-related genes *HAPLN1* and *NPPB*. RT-qPCR analysis was performed using cardioids on day 26 of differentiation from two independent batches (batch 1: A and C; batch 2: B and D). Delivery of hsa-miR-25-3p (miR-25) and hsa-miR-26a-5p (miR-26a) was performed either on day 20 of differentiation (grey) or on both days 11 and 20 of differentiation (black). Cy3-labeled miRNA was used

as a delivery control and as a negative control for gene expression. **A.** Relative *Hyaluronan and Proteoglycan Link Protein 1* (*HAPLN1)* expression following transfection with miR-25, miR-26a, or their combination (miR-25 + miR-26a) in batch 1 cardioids. **B.** Relative *HAPLN1* expression under the same conditions as A. in batch 2 cardioids. **C.** Relative *Natriuretic Peptide B* (*NPPB)* expression following delivery of miR-26a in batch 1 cardioids. **D.** Relative *NPPB* expression under the same conditions as C. in batch 2 cardioids.

Instead of a downregulation, an increase in *NPPB* expression was observed in batch 1 cardioids (**Figure 11C**). The *NPPB* gene encodes the cardioprotective hormone BNP, which is secreted under cardiac stress conditions [42]. Since its expression increased following delivery of hsa-miR-26a-5p in batch 1 cardioids, it is reasonable to hypothesize that this miRNA may have induced cardiac stress, thereby promoting BNP upregulation as a protective response.

Several factors may explain the absence of a consistent reduction in the expression of *HAPLN1* and *NPPB* genes following miRNA delivery (**Figure 11**). Firstly, in the 2D study validating miRNA-mediated silencing, only CMs were transfected [15], whereas our organoid model is composed of multiple cell types organized in a 3D architecture. Since downregulation has only been demonstrated in CMs, and RNA was extracted from all cell types within the organoid, potential silencing in CMs may have been masked by RNA derived from other cell populations (**Figure 11**). Another important difference between studies is the timing of analysis: whereas gene expression in the 2D system was assessed 24 hours after delivery [15], in our study, it was evaluated six days post-delivery (**Figure 11**). Although the presence of Cy3-labeled miRNA was still detectable at that time during delivery protocol optimization (**Figure 10C**), the miRNAs of interest may be less stable than the Cy3-labeled one, which is inert and lacks regulatory activity. It is therefore possible that the miRNAs transiently suppressed the target gene expression, but that this effect was lost as the molecules degraded, resulting in normalized expression levels by the time of the analysis (**Figure 11**).

Moreover, the results may be explained by off-target interactions, as a single miRNA is capable of regulating a broad range of mRNA transcripts [91]. Compensatory tissue responses from non-CM populations – since downregulation in CMs has already been validated in 2D cultures [15] – may have also contributed. In this context, gene silencing in CMs may have been counterbalanced by an increased expression in other cell types within the tissue. This compensatory effect might have been more pronounced for *NPPB* and could explain the gene expression increase observed in batch 1 cardioids (**Figure 11C**). Furthermore, the absence of detectable downregulation could potentially be overcome through refinement of the delivery protocol, particularly miRNA concentration and the timing and frequency of delivery. Finally, inter- and intra-batch variability, recognized as limitations of organoid systems, together with the low number of biological replicates (n=2 batches, 8-11 cardioids per condition), highlight opportunities for improvement in further studies and may explain why statistical significance was not achieved [72], [73].

3.4.2. Fibrosis-related effects of miRNA delivery

The HFpEF-associated miRNAs delivered in this work may contribute to fibrotic remodeling, potentially through the downregulation of *NPPB*, which encodes BNP – shown to exert antifibrotic effects in human CFs exposed to TGF-β [44] – and *HAPLN1*, which encodes a protein involved in ECM remodeling [15], [41]. Since such downregulation may have occurred but remained undetected, and given that our cardioid model provides a reliable platform for studying fibrosis-related cardiac conditions, we assessed the impact of miRNA delivery on cardiac tissue remodeling, with a particular focus on fibrosis. To this end, we analyzed α-SMA expression and collagen deposits – previously validated markers of CF activation and ECM accumulation in our cardioid model – to determine whether the delivery of hsa-miR-25-3p and hsa-miR-26a-5p promoted these processes (**Figure 12**).

Representative immunofluorescence and MT staining images of cardioids following miRNA delivery are shown in **Figure 12**. For miRNA delivery on day 20 of differentiation, α-SMA staining was slightly increased in the hsa-miR-26a-5p condition compared to the control, suggesting increased CF activation (**Figure 12A**). MT staining revealed collagen deposits across all conditions, indicated by black arrows, without evident differences between groups (**Figure 12A**). Quantification of α-SMA expression and collagen deposits for delivery on day 20 of differentiation did not reveal statistically significant differences between conditions (**Figure 12C**). When miRNAs were delivered on days 11 and 20, α-SMA staining was less intense in the control and slightly more pronounced in the other conditions, suggesting a higher CF activation under repeated deliveries (**Figure 12B**). MT staining revealed collagen deposits in all conditions, indicated by black arrows, without evident differences (**Figure 12B**). Quantification of α-SMA expression for delivery on days 11 and 20 of differentiation showed higher levels of α-SMA expression in two of the conditions (hsa-miR-25-3p and hsa-miR-26a-5p) when compared to the control, suggesting increased CF activation (**Figure 12D**). Nevertheless, the difference between the control and these conditions did not reach statistical significance, which was also the case for quantification of collagen deposits (**Figure 12D**).

As discussed in Chapter 3.4.1, the downregulation of the target genes *HAPLN1* and *NPPB* may have occurred but was difficult to detect (**Figure 11**). In batch 2 cardioids, a decrease in *HAPLN1* expression was previously observed when the delivery was performed twice, suggesting a cumulative effect of repeated deliveries (**Figure 11B**). Consistently, in the present experiments, overexpression of hsa-miR-25-3p and hsa-miR-26a-5p promoted CF activation under repeated deliveries (**Figure 12D**). However, in both cases, the results did reach statistical significance (**Figure 11** and **Figure 12D**).

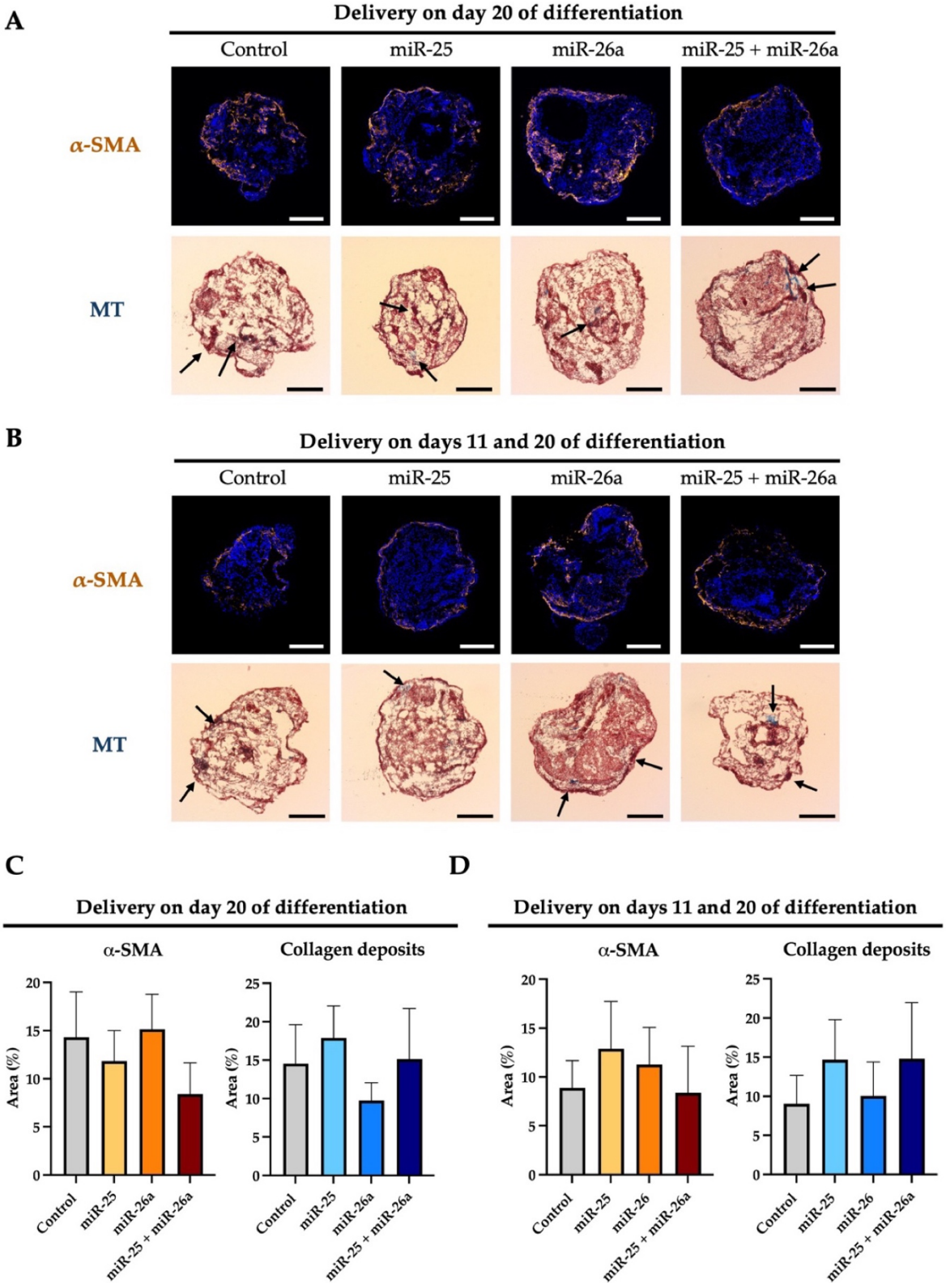

Figure 12: Immunofluorescence and MT staining following miRNA delivery, with quantification of α-SMA and collagen deposition. A. Cryosection images of cardioids on day 26 of differentiation, following delivery of Cy3-labeled miRNA, hsa-miR-25-3p (miR-25) and/or hsa-miR-26a-5p (miR-26a) on day 20. Immunofluorescence staining (top) shows activated fibroblasts (α-smooth muscle actinin (α-SMA); orange), with nuclei counterstained with

DAPI (blue). Masson's Trichrome staining (MT, bottom) shows collagen fibers (blue), cytoplasm (red), and nuclei (dark red). Black arrows indicate regions with evident collagen deposition. Scale bar = 200 μm. **B.** Cryosection images of cardioids on day 26 of differentiation, following delivery of Cy3-labeled miRNA, miR-25 and/or miR-26a on both days 11 and 20. Staining as described in A. Scale bar = 200 μm. **C.** Quantification of α-SMA (left) and collagen deposition (right), normalized to total organoid area, in cardioids following delivery of miR-25 (yellow/light blue), miR-26 (orange/blue), or both (red/dark blue) on day 20 of differentiation, together with control cardioids (Cy3-labeled miRNA, grey). Data are shown as mean ± SD (n=4 for α-SMA; n=4 for control and miR-26a, and n=3 for miR-25 and miR-25 + miR-26a in collagen deposits analysis). One-way ANOVA followed by Tukey's multiple comparisons test revealed no statistically significant differences ($p > 0.05$). **D.** Quantification of α-SMA (left) and collagen deposition (right), normalized to total organoid area, in cardioids following delivery of miR-25 (yellow/light blue), miR-26 (orange/blue), or both (red/dark blue) on both days 11 and 20, together with control cardioids (Cy3-labeled miRNA, grey). Data are shown as mean ± SD (n=3 for α-SMA; n=4 for control and miR-26a, and n=3 for miR-25 and miR-25 + miR-26a in collagen deposits analysis). One-way ANOVA followed by Tukey's multiple comparisons test revealed no statistically significant differences ($p > 0.05$).

Taken together, these findings suggest that optimization of delivery timing and frequency, combined with adjusted miRNA concentration, may enable the delivered miRNAs to exert statistically significant effects on target gene expression, as well as on fibrosis-related processes. Finally, intra-batch variability characteristic of organoid systems, together with the reduced number of cardioids per condition (n=3-4) may have limited statistical robustness of the results [73]. Importantly, increasing the number of cardioids per condition could mitigate this variability limitation and allow the detection of statistically significant effects of these miRNAs.

4

CONCLUSION AND FUTURE PERSPECTIVES

In this thesis, a cardioid model was successfully established, recapitulating the major cardiac cell types – CMs, CFs, and ECs – organized within a tissue-like architecture with vessel-like structures, and displaying functional characteristics of the native heart, such as contractile activity. The responsiveness of this cardioid model to fibrosis-related stimuli was evaluated through TGF-β treatment, a key inducer of the activation of CFs into CMFs, the main effector cells in cardiac fibrosis. This treatment induced CF activation, evidenced by increased α-SMA expression, and promoted collagen production and its accumulation, evidenced by a statistically significant increase in collagen deposits. These findings demonstrate the suitability of our cardioid model as a platform for studying fibrosis-related cardiac conditions and suggest its potential as an *in vitro* model for HFpEF, given that fibrosis represents a key underlying mechanism of this syndrome. Accordingly, miRNA delivery into cardioids was optimized to enable the delivery of HFpEF-related miRNAs. Liposomal- and electroporation-based approaches were evaluated, with liposomal-based delivery using 1 μM miRNA and serum supplementation after complex formation providing the highest delivery efficiency. Cryosection analysis confirmed the durability of this delivery approach, with Cy3-labeled miRNA fluorescence detectable for at least six days and effectively distributed into the inner regions of the organoid.

The HFpEF-related miRNAs hsa-miR-25-3p and hsa-miR-26a-5p – recently identified by our laboratory as upregulated in HFpEF and validated to downregulate *HAPLN1* and *NPPB* mRNAs in 2D CM cultures – were delivered into cardioids either on day 20 of differentiation or on both days 11 and 20. RT-qPCR analysis of cardioids from two independent batches suggested a reduction in *HAPLN1* expression under repeated delivery in one batch. However, no statistically significant reduction of *HAPLN1* or *NPPB* was observed overall. Given that downregulation may have occurred but remained undetected, we subsequently evaluated the effects of miRNA delivery on fibrosis-related mechanisms. Repeated delivery

was suggested to increase CF activation, as indicated by higher α-SMA expression in the hsa-miR-25-3p and hsa-miR-26a-5p conditions compared to the control. Nonetheless, these differences did not reach statistical significance.

To clarify the role of hsa-miR-25-3p and hsa-miR-26a-5p in CF activation and ECM deposition, potentially through the downregulation of *HAPLN1* and *NPPB*, future studies must first demonstrate the downregulation of these genes. As the multicellular composition of cardioids may mask cell-type-specific responses, it would be informative to analyze gene expression across distinct cardiac populations, for instance, using single-cell RNA sequencing, thereby enabling the identification of the specific cells in which downregulation is occurring. This would confirm whether downregulation is taking place in CMs, as previously validated in 2D. Moreover, to avoid overlooking transient regulatory effects that may have already dissipated by the time of the analysis, cardioids should be harvested at multiple time points and systematically assessed for *HAPLN1* and *NPPB* expression, rather than relying on a single evaluation.

Additionally, further optimization of the delivery protocol should be considered, particularly regarding delivery timing and frequency, and miRNA concentration. In line with this, it would be of interest to assess *HAPLN1* and *NPPB* expression throughout the differentiation protocol. This would enable the confirmation of gene expression during different stages of differentiation and the identification of the most suitable time points for miRNA delivery. Moreover, since repeated delivery was suggested to promote *HAPLN1* downregulation and CF activation, performing additional deliveries may further potentiate these effects. Furthermore, increasing the number of cardioids per condition would help mitigate the intra- and inter-batch variability inherent to organoid systems and contribute to greater statistical robustness of the results.

If downregulation is still not observed in CMs, constitutive knockdown strategies may provide a more reliable approach to investigate how these genes contribute to cardiac remodeling. In the case where downregulation of *HAPLN1* and *NPPB* is confirmed but the delivery of hsa-miR-25-3p and hsa-miR-26a-5p does not promote CF activation and ECM deposition, it is plausible to hypothesize that the effects of these miRNAs in HFpEF may be amplified by the presence of additional stimuli associated with the underlying comorbidities. Accordingly, combining their delivery with stimuli that mimic such conditions – obesity (e.g., obesity-related inflammation by cytokines), diabetes (e.g., high glucose concentration), and hypertension (e.g., angiotensin-II and endothelin-1) [83] – could uncover potential synergistic effects that more faithfully reproduce HFpEF pathophysiology, further advancing the establishment of this *in vitro* model.

Furthermore, fibrosis characterization in our cardioid model should be expanded to include a broader panel of fibrosis markers, which could be analyzed by RT-qPCR, thereby enabling a more comprehensive and reliable assessment of fibrotic processes. Examples of such markers include *PAI-1*, which encodes a protease inhibitor, and *POSTN*, which encodes periostin, an ECM protein that promotes matrix production and stabilization; both are known to be upregulated during FMT [19], [92]. In parallel, electrophysiological characterization of control and TGF-β-treated cardioids, using, for example, a multi-electrode array, would enable assessment of the functional impact of fibrosis.

An important future application of this model is drug screening for the discovery of effective therapies for HFpEF, enabling the testing of compounds directly in human cells and the evaluation of their effects on fibrotic responses at both the molecular and functional levels. In this context, promising candidates could include anti-miRNA molecules targeting hsa-miR-25-3p and hsa-miR-26a-5p, if future studies demonstrate their ability to significantly reduce the expression of fibrotic markers (e.g., α-SMA and collagen deposits) and restore the electrophysiological properties of cardioids.

Overall, this work contributed to the establishment of an HFpEF *in vitro* model by generating cardioids that structurally and functionally resemble the human heart and are responsive to fibrosis-associated stimuli. This responsiveness, together with the characterization of fibrosis within this model, represents an important step forward, since fibrosis is a key HFpEF underlying mechanism, contributing to myocardial stiffness. In addition, we established a protocol for miRNA delivery into 3D cardiac systems, providing a valuable foundation that can be further refined and applied in future studies to evaluate miRNA-related effects in cardioids.

BIBLIOGRAPHY

[1] H. Fukuta and W. C. Little, "The Cardiac Cycle and the Physiologic Basis of Left Ventricular Contraction, Ejection, Relaxation, and Filling," *Heart Fail Clin*, vol. 4, no. 1, pp. 1–11, Jan. 2008, doi: 10.1016/j.hfc.2007.10.004.

[2] G. Savarese, P. M. Becher, L. H. Lund, P. Seferovic, G. M. C. Rosano, and A. J. S. Coats, "Global burden of heart failure: a comprehensive and updated review of epidemiology," *Cardiovasc Res*, vol. 118, no. 17, pp. 3272–3287, Jan. 2023, doi: 10.1093/cvr/cvac013.

[3] R. H. G. Schwinger, "Pathophysiology of heart failure," *Cardiovasc Diagn Ther*, vol. 11, no. 1, pp. 263–276, Feb. 2021, doi: 10.21037/cdt-20-302.

[4] P. Ponikowski *et al.*, "2016 ESC Guidelines for the diagnosis and treatment of acute and chronic heart failure," *Eur Heart J*, vol. 37, no. 27, pp. 2129–2200, Jul. 2016, doi: 10.1093/eurheartj/ehw128.

[5] M. A. Pfeffer, A. M. Shah, and B. A. Borlaug, "Heart Failure With Preserved Ejection Fraction In Perspective," *Circ Res*, vol. 124, no. 11, pp. 1598–1617, May 2019, doi: 10.1161/CIRCRESAHA.119.313572.

[6] M. Rech, A. Barandiarán Aizpurua, V. van Empel, M. van Bilsen, and B. Schroen, "Pathophysiological understanding of HFpEF: microRNAs as part of the puzzle," *Cardiovasc Res*, vol. 114, no. 6, pp. 782–793, May 2018, doi: 10.1093/cvr/cvy049.

[7] L. Stoicescu, D. Crişan, C. Morgovan, L. Avram, and S. Ghibu, "Heart Failure with Preserved Ejection Fraction: The Pathophysiological Mechanisms behind the Clinical Phenotypes and the Therapeutic Approach," *Int J Mol Sci*, vol. 25, no. 2, p. 794, Jan. 2024, doi: 10.3390/ijms25020794.

[8] T. A. McDonagh *et al.*, "2021 ESC Guidelines for the diagnosis and treatment of acute and chronic heart failure," *Eur Heart J*, vol. 42, no. 36, pp. 3599–3726, Sep. 2021, doi: 10.1093/eurheartj/ehab368.

[9] W. J. Paulus and C. Tschöpe, "A Novel Paradigm for Heart Failure With Preserved Ejection Fraction," *J Am Coll Cardiol*, vol. 62, no. 4, pp. 263–271, Jul. 2013, doi: 10.1016/j.jacc.2013.02.092.

[10] S. J. Shah *et al.*, "Research Priorities for Heart Failure With Preserved Ejection Fraction," *Circulation*, vol. 141, no. 12, pp. 1001–1026, Mar. 2020, doi: 10.1161/CIRCULATIONAHA.119.041886.

[11] "NBME Internal Medicine Form 6 Explanations to Questions and Answers", Moosmosis, 2024. [Online]. Available: https://moosmosis.wordpress.com/2024/02/06/nbme-internal-medicine-form-6-explanations-to-questions-and-answers/. Accessed: Jul. 7, 2025.

[12] A. Abdin *et al.*, "Heart failure with preserved ejection fraction epidemiology, pathophysiology, diagnosis and treatment strategies," *Int J Cardiol*, vol. 412, p. 132304, Oct. 2024, doi: 10.1016/j.ijcard.2024.132304.

[13] J. Roh, N. Houstis, and A. Rosenzweig, "Why Don't We Have Proven Treatments for HFpEF?," *Circ Res*, vol. 120, no. 8, pp. 1243–1245, Apr. 2017, doi: 10.1161/CIRCRESAHA.116.310119.

[14] G. Balestrieri *et al.*, "The Therapy and Management of Heart Failure with Preserved Ejection Fraction: New Insights on Treatment," *Card Fail Rev*, vol. 10, Apr. 2024, doi: 10.15420/cfr.2023.13.

[15] J. M. Inácio *et al.*, "Myocardial RNA Sequencing Reveals New Potential Therapeutic Targets in Heart Failure with Preserved Ejection Fraction," *Biomedicines*, vol. 11, no. 8, p. 2131, Jul. 2023, doi: 10.3390/biomedicines11082131.

[16] G. D. Lopaschuk and S. Verma, "Mechanisms of Cardiovascular Benefits of Sodium Glucose Co-Transporter 2 (SGLT2) Inhibitors," *JACC Basic Transl Sci*, vol. 5, no. 6, pp. 632–644, Jun. 2020, doi: 10.1016/j.jacbts.2020.02.004.

[17] K. Schimmel, K. Ichimura, S. Reddy, F. Haddad, and E. Spiekerkoetter, "Cardiac Fibrosis in the Pressure Overloaded Left and Right Ventricle as a Therapeutic Target," *Front Cardiovasc Med*, vol. 9, May 2022, doi: 10.3389/fcvm.2022.886553.

[18] S. Hinderer and K. Schenke-Layland, "Cardiac fibrosis – A short review of causes and therapeutic strategies," *Adv Drug Deliv Rev*, vol. 146, pp. 77–82, Jun. 2019, doi: 10.1016/j.addr.2019.05.011.

[19] A. Biernacka, M. Dobaczewski, and N. G. Frangogiannis, "TGF-β signaling in fibrosis," *Growth Factors*, vol. 29, no. 5, pp. 196–202, Oct. 2011, doi: 10.3109/08977194.2011.595714.

[20] L. Zeng *et al.*, "Ubiquitin proteasome system in cardiac fibrosis," *J Adv Res*, Dec. 2024, doi: 10.1016/j.jare.2024.12.006.

[21] Y. Zhou, Y. Zhu, and J. Zeng, "Research Update on the Pathophysiological Mechanisms of Heart Failure with Preserved Ejection Fraction," *Curr Mol Med*, vol. 23, no. 1, pp. 54–62, Jan. 2023, doi: 10.2174/1566524021666211129111202.

[22] N. G. Frangogiannis, "Regulation of the Inflammatory Response in Cardiac Repair," *Circ Res*, vol. 110, no. 1, pp. 159–173, Jan. 2012, doi: 10.1161/CIRCRESAHA.111.243162.

[23] K. Maruyama and K. Imanaka-Yoshida, "The Pathogenesis of Cardiac Fibrosis: A Review of Recent Progress," *Int J Mol Sci*, vol. 23, no. 5, p. 2617, Feb. 2022, doi: 10.3390/ijms23052617.

[24] R. T. Cowling, D. Kupsky, A. M. Kahn, L. B. Daniels, and B. H. Greenberg, "Mechanisms of cardiac collagen deposition in experimental models and human disease," *Translational Research*, vol. 209, pp. 138–155, Jul. 2019, doi: 10.1016/j.trsl.2019.03.004.

[25] C. Tschöpe and S. Van Linthout, "New Insights in (Inter)Cellular Mechanisms by Heart Failure with Preserved Ejection Fraction," *Curr Heart Fail Rep*, vol. 11, no. 4, pp. 436–444, Dec. 2014, doi: 10.1007/s11897-014-0219-3.

[26] D. Ben-Nun, L. M. Buja, and F. Fuentes, "Prevention of heart failure with preserved ejection fraction (HFpEF): reexamining microRNA-21 inhibition in the era of oligonucleotide-based therapeutics," *Cardiovascular Pathology*, vol. 49, p. 107243, Nov. 2020, doi: 10.1016/j.carpath.2020.107243.

[27] Y. Tai *et al.*, "Myofibroblasts: Function, Formation, and Scope of Molecular Therapies for Skin Fibrosis," *Biomolecules*, vol. 11, no. 8, p. 1095, Jul. 2021, doi: 10.3390/biom11081095.

[28] M. D'Urso and N. A. Kurniawan, "Mechanical and Physical Regulation of Fibroblast–Myofibroblast Transition: From Cellular Mechanoresponse to Tissue Pathology," *Front Bioeng Biotechnol*, vol. 8, Dec. 2020, doi: 10.3389/fbioe.2020.609653.

[29] X. Shi, C. D. Young, H. Zhou, and X.-J. Wang, "Transforming Growth Factor-β Signaling in Fibrotic Diseases and Cancer-Associated Fibroblasts," *Biomolecules*, vol. 10, no. 12, p. 1666, Dec. 2020, doi: 10.3390/biom10121666.

[30] N. Sandbo and N. Dulin, "Actin cytoskeleton in myofibroblast differentiation: Ultrastructure defining form and driving function," *Translational Research*, vol. 158, no. 4, pp. 181–196, Oct. 2011, doi: 10.1016/j.trsl.2011.05.004.

[31] K. Saliminejad, H. R. Khorram Khorshid, S. Soleymani Fard, and S. H. Ghaffari, "An overview of microRNAs: Biology, functions, therapeutics, and analysis methods," *J Cell Physiol*, vol. 234, no. 5, pp. 5451–5465, May 2019, doi: 10.1002/jcp.27486.

[32] J. O'Brien, H. Hayder, Y. Zayed, and C. Peng, "Overview of MicroRNA Biogenesis, Mechanisms of Actions, and Circulation," *Front Endocrinol (Lausanne)*, vol. 9, Aug. 2018, doi: 10.3389/fendo.2018.00402.

[33] A. Wilczynska and M. Bushell, "The complexity of miRNA-mediated repression," *Cell Death Differ*, vol. 22, no. 1, pp. 22–33, Jan. 2015, doi: 10.1038/cdd.2014.112.

[34] W. Filipowicz, S. N. Bhattacharyya, and N. Sonenberg, "Mechanisms of post-transcriptional regulation by microRNAs: are the answers in sight?," *Nat Rev Genet*, vol. 9, no. 2, pp. 102–114, Feb. 2008, doi: 10.1038/nrg2290.

[35] J. C. Medley, G. Panzade, and A. Y. Zinovyeva, "microRNA strand selection: Unwinding the rules," *WIREs RNA*, vol. 12, no. 3, May 2021, doi: 10.1002/wrna.1627.

[36] S. Oliveto, M. Mancino, N. Manfrini, and S. Biffo, "Role of microRNAs in translation regulation and cancer," *World J Biol Chem*, vol. 8, no. 1, p. 45, 2017, doi: 10.4331/wjbc.v8.i1.45.

[37] T. F. Duchaine and M. R. Fabian, "Mechanistic Insights into MicroRNA-Mediated Gene Silencing," *Cold Spring Harb Perspect Biol*, vol. 11, no. 3, p. a032771, Mar. 2019, doi: 10.1101/cshperspect.a032771.

[38] C. J. Watson *et al.*, "MicroRNA signatures differentiate preserved from reduced ejection fraction heart failure," *Eur J Heart Fail*, vol. 17, no. 4, pp. 405–415, Apr. 2015, doi: 10.1002/ejhf.244.

[39] E. Lozano-Velasco *et al.*, "miRNAs in Heart Development and Disease," *Int J Mol Sci*, vol. 25, no. 3, p. 1673, Jan. 2024, doi: 10.3390/ijms25031673.

[40] R.-H. LIU, B. NING, X.-E. MA, W.-M. GONG, and T.-H. JIA, "Regulatory roles of microRNA-21 in fibrosis through interaction with diverse pathways (Review)," *Mol Med Rep*, vol. 13, no. 3, pp. 2359–2366, Mar. 2016, doi: 10.3892/mmr.2016.4834.

[41] J. Sun *et al.*, "*hapln1* Defines an Epicardial Cell Subpopulation Required for Cardiomyocyte Expansion During Heart Morphogenesis and Regeneration," *Circulation*, vol. 146, no. 1, pp. 48–63, Jul. 2022, doi: 10.1161/CIRCULATIONAHA.121.055468.

[42] J. Man, P. Barnett, and V. M. Christoffels, "Structure and function of the Nppa–Nppb cluster locus during heart development and disease," *Cellular and Molecular Life Sciences*, vol. 75, no. 8, pp. 1435–1444, Apr. 2018, doi: 10.1007/s00018-017-2737-0.

[43] T. NISHIKIMI, N. MAEDA, and H. MATSUOKA, "The role of natriuretic peptides in cardioprotection," *Cardiovasc Res*, vol. 69, no. 2, pp. 318–328, Feb. 2006, doi: 10.1016/j.cardiores.2005.10.001.

[44] A. M. Kapoun *et al.*, "B-Type Natriuretic Peptide Exerts Broad Functional Opposition to Transforming Growth Factor-β in Primary Human Cardiac Fibroblasts," *Circ Res*, vol. 94, no. 4, pp. 453–461, Mar. 2004, doi: 10.1161/01.RES.0000117070.86556.9F.

[45] E. C. H. van Doorn, J. H. Amesz, A. H. Sadeghi, N. M. S. de Groot, O. C. Manintveld, and Y. J. H. J. Taverne, "Preclinical Models of Cardiac Disease: A Comprehensive Overview for Clinical Scientists," *Cardiovasc Eng Technol*, vol. 15, no. 2, pp. 232–249, Apr. 2024, doi: 10.1007/s13239-023-00707-w.

[46] Z. Zhu and D. Huangfu, "Human pluripotent stem cells: an emerging model in developmental biology," *Development*, vol. 140, no. 4, pp. 705–717, Feb. 2013, doi: 10.1242/dev.086165.

[47] A. Krishnan *et al.*, "A detailed comparison of mouse and human cardiac development," *Pediatr Res*, vol. 76, no. 6, pp. 500–507, Dec. 2014, doi: 10.1038/pr.2014.128.

[48] A. Gök and E. Beyazçiçek, "Experimental Animal Models in Heart Disease," *Düzce Tıp Fakültesi Dergisi*, vol. 26, no. S1, pp. 79–86, Jun. 2024, doi: 10.18678/dtfd.1489656.

[49] S. Gao *et al.*, "Animal models of heart failure with preserved ejection fraction (HFpEF): from metabolic pathobiology to drug discovery," *Acta Pharmacol Sin*, vol. 45, no. 1, pp. 23–35, Jan. 2024, doi: 10.1038/s41401-023-01152-0.

[50] A. Schauer *et al.*, "ZSF1 rat as animal model for HFpEF: Development of reduced diastolic function and skeletal muscle dysfunction," *ESC Heart Fail*, vol. 7, no. 5, pp. 2123–2134, Oct. 2020, doi: 10.1002/ehf2.12915.

[51] B. L. F. Kaplan *et al.*, "Protecting Human and Animal Health: The Road from Animal Models to New Approach Methods," *Pharmacol Rev*, vol. 76, no. 2, pp. 251–266, Mar. 2024, doi: 10.1124/pharmrev.123.000967.

[52] A. Adegunsoye, N. M. Gonzales, and Y. Gilad, "Induced Pluripotent Stem Cells in Disease Biology and the Evidence for Their In Vitro Utility," *Annu Rev Genet*, vol. 57, no. 1, pp. 341–360, Nov. 2023, doi: 10.1146/annurev-genet-022123-090319.

[53] A. Liras, "Future research and therapeutic applications of human stem cells: general, regulatory, and bioethical aspects," *J Transl Med*, vol. 8, no. 1, p. 131, Dec. 2010, doi: 10.1186/1479-5876-8-131.

[54] A. Romito and G. Cobellis, "Pluripotent Stem Cells: Current Understanding and Future Directions," *Stem Cells Int*, vol. 2016, no. 1, Jan. 2016, doi: 10.1155/2016/9451492.

[55] J. Cerneckis, H. Cai, and Y. Shi, "Induced pluripotent stem cells (iPSCs): molecular mechanisms of induction and applications," *Signal Transduct Target Ther*, vol. 9, no. 1, p. 112, Apr. 2024, doi: 10.1038/s41392-024-01809-0.

[56] K. Takahashi and S. Yamanaka, "Induction of Pluripotent Stem Cells from Mouse Embryonic and Adult Fibroblast Cultures by Defined Factors," *Cell*, vol. 126, no. 4, pp. 663–676, Aug. 2006, doi: 10.1016/j.cell.2006.07.024.

[57] K. Takahashi *et al.*, "Induction of Pluripotent Stem Cells from Adult Human Fibroblasts by Defined Factors," *Cell*, vol. 131, no. 5, pp. 861–872, Nov. 2007, doi: 10.1016/j.cell.2007.11.019.

[58] E. Panferov *et al.*, "Induced Pluripotent (iPSC) and Mesenchymal (MSC) Stem Cells for In Vitro Disease Modeling and Regenerative Medicine," *Int J Mol Sci*, vol. 26, no. 12, p. 5617, Jun. 2025, doi: 10.3390/ijms26125617.

[59] M. Sahara, "Recent Advances in Generation of In Vitro Cardiac Organoids," *Int J Mol Sci*, vol. 24, no. 7, p. 6244, Mar. 2023, doi: 10.3390/ijms24076244.

[60] G. Campostrini *et al.*, "Generation, functional analysis and applications of isogenic three-dimensional self-aggregating cardiac microtissues from human pluripotent stem cells," *Nat Protoc*, vol. 16, no. 4, pp. 2213–2256, Apr. 2021, doi: 10.1038/s41596-021-00497-2.

[61] N. Roshanravan *et al.*, "Human cardiac organoids: A recent revolution in disease modeling and regenerative medicine," *J Cardiovasc Thorac Res*, vol. 15, no. 2, pp. 68–72, Jun. 2023, doi: 10.34172/jcvtr.2023.31830.

[62] I. Gisone, A. Cecchettini, E. Ceccherini, E. Persiani, M. A. Morales, and F. Vozzi, "Cardiac tissue engineering: Multiple approaches and potential applications," *Front Bioeng Biotechnol*, vol. 10, Oct. 2022, doi: 10.3389/fbioe.2022.980393.

[63] R. N. Gomes, M. Cardona-Timoner, E. D. Silva, A. Pombinho, and D. S. Nascimento, "A high-throughput analysis of novel anti-fibrotics in human adult cardiac fibroblasts," *Biomedicine & Pharmacotherapy*, vol. 188, p. 118216, Jul. 2025, doi: 10.1016/j.biopha.2025.118216.

[64] J. M. Inácio, M. M. Nunes, M. Almeida, F. Cristo, R. Anjos, and J. A. Belo, "Gene-Edited Human-Induced Pluripotent Stem Cell Lines to Elucidate DAND5 Function throughout Cardiac Differentiation," *Cells*, vol. 12, no. 4, p. 520, Feb. 2023, doi: 10.3390/cells12040520.

[65] S. Yang *et al.*, "Organoids: The current status and biomedical applications," *MedComm (Beijing)*, vol. 4, no. 3, Jun. 2023, doi: 10.1002/mco2.274.

[66] D. Thomas, S. Choi, C. Alamana, K. K. Parker, and J. C. Wu, "Cellular and Engineered Organoids for Cardiovascular Models," *Circ Res*, vol. 130, no. 12, pp. 1780–1802, Jun. 2022, doi: 10.1161/CIRCRESAHA.122.320305.

[67] H. Kim, R. D. Kamm, G. Vunjak-Novakovic, and J. C. Wu, "Progress in multicellular human cardiac organoids for clinical applications," *Cell Stem Cell*, vol. 29, no. 4, pp. 503–514, Apr. 2022, doi: 10.1016/j.stem.2022.03.012.

[68] X. Liu, Z. Zhou, Y. Zhang, H. Zhong, X. Cai, and R. Guan, "Recent progress on the organoids: Techniques, advantages and applications," *Biomedicine & Pharmacotherapy*, vol. 185, p. 117942, Apr. 2025, doi: 10.1016/j.biopha.2025.117942.

[69] Y. R. Lewis-Israeli *et al.*, "Self-assembling human heart organoids for the modeling of cardiac development and congenital heart disease," *Nat Commun*, vol. 12, no. 1, p. 5142, Aug. 2021, doi: 10.1038/s41467-021-25329-5.

[70] G. Novelli, P. Spitalieri, M. Murdocca, E. Centanini, and F. Sangiuolo, "Organoid factory: The recent role of the human induced pluripotent stem cells (hiPSCs) in precision medicine," *Front Cell Dev Biol*, vol. 10, Jan. 2023, doi: 10.3389/fcell.2022.1059579.

[71] Y. Huang *et al.*, "Research Progress, Challenges, and Breakthroughs of Organoids as Disease Models," *Front Cell Dev Biol*, vol. 9, Nov. 2021, doi: 10.3389/fcell.2021.740574.

[72] X. Fan, K. Hou, G. Liu, R. Shi, W. Wang, and G. Liang, "Strategies to overcome the limitations of current organoid technology - engineered organoids," *J Tissue Eng*, vol. 16, Apr. 2025, doi: 10.1177/20417314251319475.

[73] K. Gehling *et al.*, "Single organoid RNA-sequencing reveals high organoid-to-organoid variability," Nov. 22, 2021. doi: 10.1101/2021.11.22.469588.

[74] Y. R. Lewis-Israeli, A. H. Wasserman, and A. Aguirre, "Heart Organoids and Engineered Heart Tissues: Novel Tools for Modeling Human Cardiac Biology and Disease," *Biomolecules*, vol. 11, no. 9, p. 1277, Aug. 2021, doi: 10.3390/biom11091277.

[75] A. B. Meier *et al.*, "Epicardioid single-cell genomics uncovers principles of human epicardium biology in heart development and disease," *Nat Biotechnol*, vol. 41, no. 12, pp. 1787–1800, Dec. 2023, doi: 10.1038/s41587-023-01718-7.

[76] C. Balbi and N. Smart, "Epicardioids: a novel tool for cardiac regeneration research?," *Cardiovasc Res*, vol. 119, no. 17, pp. e164–e166, Dec. 2023, doi: 10.1093/cvr/cvad172.

[77] M. Song *et al.*, "Modeling acute myocardial infarction and cardiac fibrosis using human induced pluripotent stem cell-derived multi-cellular heart organoids," *Cell Death Dis*, vol. 15, no. 5, p. 308, May 2024, doi: 10.1038/s41419-024-06703-9.

[78] D. M. Lyra-Leite, Ó. Gutiérrez-Gutiérrez, M. Wang, Y. Zhou, L. Cyganek, and P. W. Burridge, "A review of protocols for human iPSC culture, cardiac differentiation, subtype-specification, maturation, and direct reprogramming," *STAR Protoc*, vol. 3, no. 3, p. 101560, Sep. 2022, doi: 10.1016/j.xpro.2022.101560.

[79] Y. Jiang, P. Park, S.-M. Hong, and K. Ban, "Maturation of Cardiomyocytes Derived from Human Pluripotent Stem Cells: Current Strategies and Limitations.," *Mol Cells*, vol. 41, no. 7, pp. 613–621, Jul. 2018, doi: 10.14348/molcells.2018.0143.

[80] H. Lee *et al.*, "Three-dimensional cardiac organoid formation accelerates the functional maturation of human induced pluripotent stem cell-derived cardiomyocytes," *Organoid*, vol. 2, p. e14, May 2022, doi: 10.51335/organoid.2022.2.e14.

[81] N. G. Frangogiannis, "The extracellular matrix in myocardial injury, repair, and remodeling," *Journal of Clinical Investigation*, vol. 127, no. 5, pp. 1600–1612, May 2017, doi: 10.1172/JCI87491.

[82] D. Sridharan, N. Pracha, J. A. Dougherty, A. Akhtar, S. B. Alvi, and M. Khan, "A One-Stop Protocol to Assess Myocardial Fibrosis in Frozen and Paraffin Sections," *Methods Protoc*, vol. 5, no. 1, p. 13, Jan. 2022, doi: 10.3390/mps5010013.

[83] I. R. Haim, A. Gruber, N. Kazma, C. Bashai, H. Lichtig Kinsbruner, and O. Caspi, "Modeling Heart Failure With Preserved Ejection Fraction Using Human Induced Pluripotent Stem Cell–Derived Cardiac Organoids," *Circ Heart Fail*, vol. 18, no. 3, Mar. 2025, doi: 10.1161/CIRCHEARTFAILURE.124.011690.

[84] B. Laperrousaz *et al.*, "Direct transfection of clonal organoids in Matrigel microbeads: a promising approach toward organoid-based genetic screens," *Nucleic Acids Res*, vol. 46, no. 12, pp. e70–e70, Jul. 2018, doi: 10.1093/nar/gky030.

[85] G. L. Prasanna and T. Panda, "Electroporation: basic principles, practical considerations and applications in molecular biology," *Bioprocess Engineering*, vol. 16, no. 5, p. 261, 1997, doi: 10.1007/s004490050319.

[86] Z. X. Chong, S. K. Yeap, and W. Y. Ho, "Transfection types, methods and strategies: a technical review," *PeerJ*, vol. 9, p. e11165, Apr. 2021, doi: 10.7717/peerj.11165.

[87] T. K. Kim and J. H. Eberwine, "Mammalian cell transfection: the present and the future," *Anal Bioanal Chem*, vol. 397, no. 8, pp. 3173–3178, Aug. 2010, doi: 10.1007/s00216-010-3821-6.

[88] L. Broutier *et al.*, "Culture and establishment of self-renewing human and mouse adult liver and pancreas 3D organoids and their genetic manipulation," *Nat Protoc*, vol. 11, no. 9, pp. 1724–1743, Sep. 2016, doi: 10.1038/nprot.2016.097.

[89] Q. Kong *et al.*, "A transfection method of PS-asODNs targeting ANGPTL4 in multicellular structures of hepatocarcinoma cell line," *Cancer Gene Ther*, vol. 22, no. 5, pp. 285–290, May 2015, doi: 10.1038/cgt.2015.22.

[90] R. G. Morgan, A. C. Chambers, D. N. Legge, S. J. Coles, A. Greenhough, and A. C. Williams, "Optimized delivery of siRNA into 3D tumor spheroid cultures in situ," *Sci Rep*, vol. 8, no. 1, p. 7952, May 2018, doi: 10.1038/s41598-018-26253-3.

[91] C. Diener, A. Keller, and E. Meese, "Emerging concepts of miRNA therapeutics: from cells to clinic," *Trends in Genetics*, vol. 38, no. 6, pp. 613–626, Jun. 2022, doi: 10.1016/j.tig.2022.02.006.

[92] M. Nemir *et al.*, "The Notch pathway controls fibrotic and regenerative repair in the adult heart," *Eur Heart J*, vol. 35, no. 32, pp. 2174–2185, Aug. 2014, doi: 10.1093/eurheartj/ehs269.

A

APPENDIX

A.1. miRNA sequences

Table A1: miRNA sequences.

miRNA	Mature sequence
hsa-miR-25-3p	5′ CAUUGCACUUGUCUCGGUCUGA 3′
hsa-miR-26a-5p	5′ UUCAAGUAAUCCAGGAUAGGCU 3′

A.2. Antibodies used for immunofluorescence staining

Table A2: Primary and secondary antibodies used for immunofluorescence.

	Target	Host species	Manufacturer	Catalog number	Dilution
Primary	Vimentin	Rabbit	Cell Signaling	5741	1:200
	α-actinin	Mouse	Sigma-Aldrich	A7811	1:500
	VE-Cadherin	Rabbit	Abcam	AB11256	1:600
	α-SMA	Mouse	Dako	M0851	1:600
	COL1A1	Rabbit	Cell Signaling	39952	1:400
Secondary	Alexa Fluor 488	Donkey (anti-rabbit)	Invitrogen	A21206	1:250
	Alexa Fluor 594	Donkey (anti-mouse)	Invitrogen	A21203	1:250

A.3. RT-qPCR primers

Table A3: Forward and reverse primer sequences used in RT-qPCR with corresponding annealing temperatures.

Target gene	Primer sequence	Annealing temperature (°C)
HAPLN1	Fwd 5′ GATACTGTTGTGGTAGCACTGG 3′	59.8
	Rev 5′ TGCTGCGCCTCGTGAAAATTGAG 3′	
NPPB	Fwd 5′ CCCCGGTTCAGCCTCGGACT 3′	60
	Rev 5′ ACGGATGCCCTCGGTGGCTA 3′	
GAPDH	Fwd 5′ GCTGGTAAAGTGGATATTGTTGCCAT 3′	57.9
	Rev 5′ TGGAATCATATTGGAACATGTAAACC 3′	